Closed Mesoscale Cellular Convection Driven by Cloud-Top Radiative Cooling

QINGQIU SHAO

Institute of Atmospheric Physics, The University of Arizona, Tucson, Arizona

DAVID A. RANDALL

Department of Atmospheric Science, Colorado State University, Fort Collins, Colorado

(Manuscript received 7 July 1995, in final form 30 January 1996)

ABSTRACT

Closed mesoscale cellular convection (MCC) consists of mesoscale cloud patches separated by narrow clear regions. Strong radiative cooling occurs at the cloud top. In this study a dry two-dimensional Boussinesq model is used to study the effects of cloud-top cooling on convection. Wide updrafts and narrow downdrafts are used to indicate the asymmetric circulations associated with the mesoscale cloud patches. Linear analysis of the model indicates only that the longest waves are most unstable and gives no indication of asymmetric convection cells in the linear convective regime. A weakly nonlinear analysis suggests the presence of downdrafts that are narrower than the updrafts, but this effect is not very pronounced for reasonable values of parameters. Fully nonlinear numerical simulations show that strong cloud-top cooling can generate highly asymmetric mesoscale cells corresponding to closed MCC. Nonlinear processes play essential roles in generating and maintaining closed MCC. The effects of cloud-top radiative cooling on the model dynamics can only be fully represented in a fully nonlinear model. Based on the numerical results, a conceptual model is constructed to suggest a mechanism for the formation of closed MCC over cool ocean surfaces.

1. Introduction

Satellite observations often show that stratocumulus clouds over the oceans are composed of mesoscale cloud patches that are separated by narrow clear regions. An example is shown in Fig. 1, which was obtained during the Atlantic Stratocumulus Transition Experiment (ASTEX, e.g., Albrecht et al. 1995). The cloud patches have horizontal scales of tens of kilometers, so that their aspect ratio [the distance between two adjacent cloud patch centers divided by the depth of the stratocumulus-topped boundary layer (STBL)] is in the range 15–30 (e.g., Agee 1987). Since the cloud patches often exhibit hexagonal patterns, they are referred to as "closed" mesoscale cellular convection (MCC) (Krueger and Fritz 1961; Hubert 1966), in contrast to "open" MCC in which clear mesoscale cells are surrounded by narrow cloudy regions formed by cumuli. Although closed MCC are sometimes observed over warm ocean currents on the western sides of the oceans, in association with cold air outbreaks (Lenschow and Agee 1976; Rand 1995), closed MCC is more frequently observed over the cold ocean currents of the eastern subtropical oceans (e.g., Agee et al. 1973; Agee and Lomax 1978), as for the case shown in Fig. 1.

Mechanisms for the formation of closed MCC over the subtropical oceans have not yet been fully explored. Due to the resemblance of the pattern of MCC to that of classical Benard–Rayleigh (B–R) convection, various mechanisms for MCC have been devised by modifying B–R theory, that is, by adding to the theory the physical processes that are (or might be) unique to the atmosphere, such as anisotropic turbulent diffusion, large-scale vertical motion, latent heat release, vertically asymmetric internal heating, wave–convection interactions, particular top and bottom boundary conditions, and mesoscale entrainment instability [see reviews by, e.g., Agee et al. (1973), Agee (1987), Shao (1994), Rand (1995), and references therein]. However, none of the proposed mechanisms has explained satisfactorily both the distinct features of closed MCC, that is, circulations associated with the wide cloudy regions and narrow clear regions, and the large aspect ratio.

With a large cloud amount of about 90% (e.g., Agee 1987), cloud-top radiative cooling plays an important role in driving convection in the STBL (e.g., Shao 1994). Helfand and Kalnay (1983) studied the effects of asymmetric internal heating–cooling on the direction of the convective circulations. Through a numerical study of a B–R type model with zero-heat-flux

Corresponding author address: Dr. Qingqiu Shao, Institute of Atmospheric Physics, The University of Arizona, PAS Bldg., #81, Tucson, AZ 85721.
E-mail: Qingqiu@stratus.atmo.arizona.edu

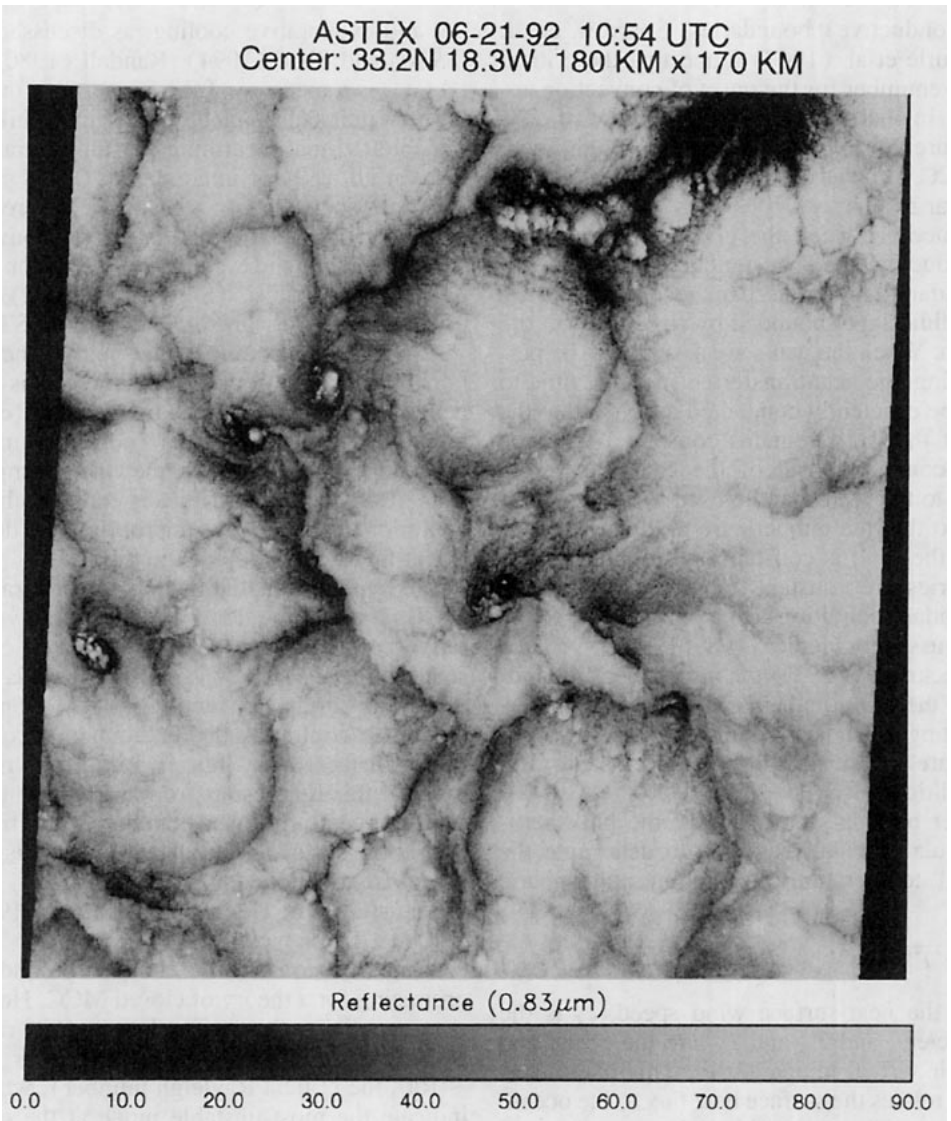

FIG. 1. The mesoscale cloud patches observed during ASTEX (provided by B. A. Wielicki).

boundary conditions (no net heating), they found that with a high Rayleigh number ($Ra = 10^5$), strong cooling concentrated in the upper part of the layer can generate closed circulations, while strong warming concentrated in the lower part of the layer can generate open circulations. Their results suggest that radiative and evaporative cooling at cloud top may be the driving force for closed MCC. However, their conclusion about MCC was constrained by their domain size.

An intrinsic problem in using a B–R model to study MCC is that the aspect ratio of classical B–R convection is about an order of magnitude smaller than that of MCC. Linear analysis (e.g., Chandrasekhar 1961; Rothermel and Agee 1986; Sheu et al. 1980) shows that the constant-temperature (or perfectly conductive) boundary condition in the classical R–B theory only allows a small aspect ratio (~ 3) for the most unstable mode. Sasaki (1970) first noticed that the top and bottom boundaries of atmospheric boundary layers in which MCC occurs are not necessarily at constant temperature but possibly have constant heat fluxes. In a linear analysis of the B–R problem with constant heat

flux (or nonconductive) boundaries, Sparrow et al. (1964) and Hurle et al. (1967) found that the critical horizontal wavenumber for the onset of convection approaches zero, in sharp contrast with the case of constant temperature. Sasaki (1970) did a thorough linear analysis of MCC with various boundary conditions and obtained similar results.

The differences between the constant temperature (perfectly conducting) and constant heat flux (nonconductive) boundary conditions can be understood by considering a fluid layer bounded by rigid walls at the top and bottom. When the walls are assumed to be perfectly conducting, the heat transferred from the fluid to the walls can be efficiently conducted away so that the temperature of the walls remains constant. When the walls are nonconductive, all of the heat transferred from the fluid to the walls can be used to change their temperature, so that the temperature gradient between the walls and the fluid is constant and the heat fluxes at the boundaries are constant. Obviously neither of these two boundary conditions can apply exactly to the STBL. As discussed by Fiedler (1989, 1990, 1993) and Fiedler and Peckman (1992), the atmospheric boundary layer over the ocean is better described by imperfectly conducting boundary conditions (neither constant temperature nor constant flux) but is closer to constant flux condition.

At the lower boundary of a STBL, the bulk aerodynamic formula is usually applied to determine the surface virtual temperature flux in an atmospheric model; that is,

$$\overline{w'T'_{vS}} = |\mathbf{V}|_S c_T (T_{vS} - T_{vA}). \quad (1)$$

Here $|\mathbf{V}|_S$ is the near-surface wind speed, c_T is the transfer coefficient, and T_{vS} and T_{vA} are the ocean and near-surface air virtual temperatures. This parameterization clearly relates the surface heat flux to the ocean-air temperature difference, although complications arise due to the fact that c_T generally depends on stability. Since the ocean has a large heat capacity, T_{vS} can be considered to be fixed, and so (1) corresponds to the "constant temperature" boundary condition.

In contrast, as discussed by Lilly (1968), at the top of the STBL the virtual temperature flux is determined in part by the entrainment rate, which leads to both warming due to the downward flux of warm air and cooling due to evaporation and in part by the radiative cooling rate; that is,

$$\rho c_p \overline{w'T'_{vB}} = -E[\Delta s_v - (\Delta s_v)_{\text{crit}}] + \beta \Delta R. \quad (2)$$

Here ρ is the air density, c_p is the heat capacity at constant pressure, E is the entrainment mass flux, $[\Delta s_v - (\Delta s_v)_{\text{crit}}]$ is a measure of the "jumps" of both temperature and moisture across the top of the STBL, β is a positive nondimensional coefficient, and ΔR is the radiative jump across the STBL top. The entrainment term of (2) includes the effects of both sensible warming and evaporative cooling, as discussed by Randall (1980) and Shao (1994). Randall (1980) shows that $(\Delta s_v)_{\text{crit}}$ is a measure of the evaporative (virtual) cooling per unit entrainment mass flux, while Δs_v is the sensible (virtual) warming per unit entrainment mass flux. In all cases of interest both $(\Delta s_v)_{\text{crit}}$ and Δs_v are positive. The radiation term of (2) represents the effects of radiative cooling that drives convection since $\Delta R > 0$. This corresponds to very strong cooling of the order of 10 K h^{-1} (Slingo et al. 1982) concentrated in a thin layer near the cloud top of an STBL.

The important point is that neither the evaporative nor the radiative cooling at cloud top is strongly dependent on the above-cloud temperature (especially the radiative cooling), and so a "constant flux" boundary condition is appropriate for the virtual temperature flux. This strongly suggests that a constant-flux boundary condition is physically appropriate to determine the "heat flux" at the top of the STBL.

We hypothesize that the large aspect ratio of closed MCC is due to the dominance of radiative and evaporative cooling at the STBL top, which can be represented in terms of a constant-flux boundary condition. Since our study concentrates on motions driven by cloud-top cooling, a lower boundary condition with weak surface heat flux is preferred, regardless of whether this flux results from the constant-flux or constant-temperature lower boundary condition. We simply set the surface heat flux to zero in this study unless otherwise mentioned.

The studies of Helfand and Kalnay (1983) and Sasaki (1970) suggest that a combination of cloud-top cooling with constant-flux boundary conditions seems promising for a theory of closed MCC. However, there is a potential problem. The large aspect ratio obtained by Sasaki (1970) is based on the linear analysis (Ra $\sim$ Ra_c, the critical Rayleigh number), which can only indicate the most unstable mode at the *onset* of convection. The closed-type circulation obtained by Helfand and Kalnay (1983), on the other hand, comes from a fully nonlinear numerical solution (Ra $\gg$ Ra_c), which represents fully developed convection. Therefore, the large aspect ratio and the closed-type circulations were obtained for different convection regimes. Questions naturally arise. First, can cloud-top cooling produce closed-type circulations in *linear* models? Second, can the preferred aspect ratio of the linear model still dominate in fully developed convection with and without cloud-top cooling?

To answer these questions, we need a model that is simple enough to do analytical studies but complex enough to represent the relevant nonlinear effects. For this purpose we adopt a two-dimensional (2D) Boussinesq model with constant-flux boundary conditions and cloud-top cooling. Large-scale vertical motion is not considered. The idealized, prescribed internal heating–cooling profile is interpreted in terms of cloud-top radiative cooling. The entrainment rate is set to zero so

that the domain height represents the height of the STBL top. Since no moisture exists in the model, we assume for purposes of interpretation only that clouds are associated with updrafts and clear regions are associated with downdrafts. Thus closed MCC in our model is indicated by wide updrafts and narrow downdrafts. This is consistent with the results obtained by Rothermel and Agee (1980) from aircraft observations and Helfand and Kalnay (1983) from their modeling studies.

Real MCC is, of course, a three-dimensional (3D) phenomenon. Fiedler (1993) and Fiedler and Khairoutdinov (1994) suggest that a 3D model is necessary to simulate MCC because mesoscale cells do not appear in their 2D simulations but do appear in their 3D simulations. The difference of the energy cascades between 2D and 3D convection does not matter for linear analyses. For nonlinear numerical simulations, cloud-top cooling dominates the 2D anticascade process in generating closed MCC in our model, as discussed in section 4 and section 5.

In this paper we perform both linear and weakly nonlinear analyses, as well as fully nonlinear numerical simulations, to reveal how cloud-top cooling drives closed MCC. The equations are presented in section 2. A linear analysis of the model is given in section 3, and a finite-amplitude "weakly nonlinear" analysis is presented in section 4. Nonlinear numerical simulations are discussed in section 5. Concluding remarks are given in section 6.

2. The model

The 2D Boussinesq equations without the Coriolis effect can be written in "vorticity form" as

$$\zeta = \frac{\partial^2\psi}{\partial x^2} + \frac{\partial^2\psi}{\partial z^2},$$

$$\frac{\partial\zeta}{\partial t} - \frac{\partial\psi}{\partial z}\frac{\partial\zeta}{\partial x} + \frac{\partial\psi}{\partial x}\frac{\partial\zeta}{\partial z} = \frac{g}{\Theta_0}\frac{\partial\theta}{\partial x} + K_M\left(\frac{\partial^2\zeta}{\partial x^2} + \frac{\partial^2\zeta}{\partial z^2}\right),$$

$$\frac{\partial\theta}{\partial t} - \frac{\partial\psi}{\partial z}\frac{\partial\theta}{\partial x} + \frac{\partial\psi}{\partial x}\frac{\partial\theta}{\partial z} = \dot{Q} + K_H\left(\frac{\partial^2\theta}{\partial x^2} + \frac{\partial^2\theta}{\partial z^2}\right), \quad (3)$$

where $\Theta_0 = 300$ K is the reference potential temperature, θ is the fluctuation of potential temperature, ψ is the streamfunction, $\zeta = \partial w/\partial x - \partial u/\partial z$ is the vorticity, and $u = -\partial\psi/\partial z$, $w = \partial\psi/\partial x$ are the fluctuations of the wind components. Note that the streamfunction and vorticity defined here have opposite signs as those defined conventionally. The turbulent transfer coefficients, K_M for momentum and K_H for heat, are constants. The quantity $\dot{Q}$ represents the prescribed internal heating–cooling profile and is height dependent. The horizontal and vertical coordinates are x and z.

The lower and upper boundary conditions are

$$u = 0, \quad w = 0 \quad \left(\text{or } \frac{\partial\psi}{\partial z} = 0, \psi = 0\right), \quad \text{and} \quad \frac{\partial\theta}{\partial z} = c_b \quad \text{at} \quad z = 0; \quad (4)$$

$$\frac{\partial u}{\partial z} = 0, \quad w = 0 \quad \left(\text{or } \frac{\partial^2\psi}{\partial z^2} = 0, \psi = 0\right), \quad \text{and} \quad \frac{\partial\theta}{\partial z} = c_t \quad \text{at} \quad z = d. \quad (5)$$

Here d is the depth of the STBL. The constants c_b and c_t represent constant heat fluxes at the boundaries. The lower boundary is rigid and nonslip, and the upper boundary is rigid and free slip. The lateral boundaries are assumed to be periodic.

The driving forces of the system are the internal heating–cooling and the heat fluxes at the upper and lower boundaries. For a steady state, the thermodynamic equation gives the relationship between the driving forces as

$$\int_0^d \dot{Q}dz = K_H(c_b - c_t). \quad (6)$$

We prescribe the profile of $\dot{Q}$ following Helfand and Kalnay (1983):

$$\dot{Q} = a[(z_0/d)^n - (z/d)^n]. \quad (7)$$

Here d is the depth of the STBL, and $n \geq 1$. Term $\dot{Q}$ changes linearly with height when $n = 1$. For a positive a, $\dot{Q} > 0$ for $z < z_0$ and $\dot{Q} < 0$ for $z > z_0$. Thus, $a > 0$ is necessary to represent cloud-top cooling. The condition

$$\int_0^d \dot{Q}dz = 0 \quad (8)$$

is imposed so that the net internal heating–cooling is zero. Thus the positive flux, $F(n)$, for $z < z_0$ is equal to the negative flux for $z > z_0$; that is,

$$F(n) \equiv \int_0^{z_0} \dot{Q}dz = -\int_{z_0}^d \dot{Q}dz > 0. \quad (9)$$

Equations (6)–(9) give

$$z_0 = d\left(\frac{1}{n+1}\right)^{1/n}, \quad (10)$$

$$a = \frac{F(n)}{nd}(n+1)^{(2n+1)/n}, \quad (11)$$

and

$$-K_Hc_b + F(n) = -K_Hc_t + F(n). \quad (12)$$

Equation (12) states that $c_b = c_t$. When $c_b = c_t = 0$, the heat fluxes at the boundaries are zero, so that the

flux $F(n)$ is the only heat source that can drive motions. In this study, we let

$$F_0 \equiv -K_H c_b + F(n) \tag{13}$$

be a constant, so that the total heat input is the same for all the cases studied. Accordingly, F_0 can be employed as a scaling parameter for temperature.

There are three possible situations, depending on the ways that $F(n)$ and $K_H c_b$ enter in (13), that is, 1) $K_H c_b = 0$, $F(n) = F_0$; 2) $K_H c_b = -F_0$, $F(n) = 0$; and 3) both internal and boundary heating–cooling exist. Our study concentrates on the first situation. It is analyzed linearly to address the first question raised in section 1, that is, the role of radiative cooling in the linear and weakly nonlinear convection regime. A linear analysis of the second situation was presented by Sasaki (1970). All three situations will be analyzed for the weakly nonlinear regime and simulated for the fully nonlinear regime in order to address the second question, that is, whether and how radiative cooling generates closed MCC through nonlinear processes.

Five cases have been designed based on the above three situations, as shown in Fig. 2. The parameters are listed in Table 1. We assume that $F_0 = 0.23$ K m s^{-1} (or ~230 W m^{-2}) and $d = 1500$ m, as in a typical STBL. Cases 1–3 are for the first situation, with n adjusted so that the strength of cloud-top cooling changes. When n is large, the strong cooling is concentrated in the layer $z > z_0$, while mild warming is spread over a deep layer where $z < z_0$. Cases 4 and 5 are for the second and third situations, respectively.

3. Linear analysis

By substituting

$$\psi = \hat{\psi} K_M,$$
$$\theta = \hat{\theta} F_0 d / K_H,$$
$$t = \hat{t} d^2 / K_H,$$

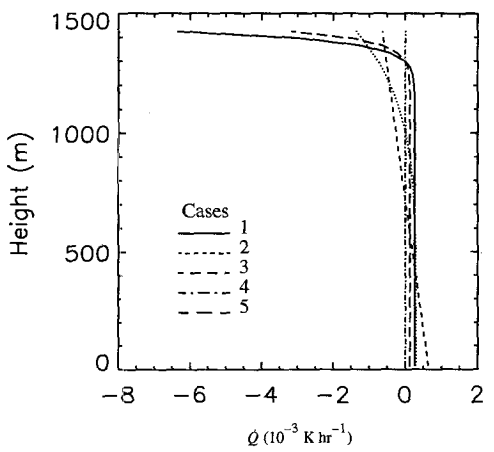

FIG. 2. The internal heating–cooling profiles for the five cases listed in Table 1.

TABLE 1. The parameters for prescribing the internal–boundary driving force. Cases 1 to 3 only have internal forcing. Case 4 has only boundary forcing, and case 5 has both internal and boundary forcing.

Case	n	a (10^{-3} K s^{-1})	z_0/d	F (K m s^{-1})	c_b (K m^{-1})
1	35	6.636	0.9	0.23	0
2	5	1.667	0.7	0.23	0
3	1	1.294	0.5	0.23	0
4	—	0	—	0	$-0.23/K_H$
5	35	3.318	0.9	0.115	$-0.115/K_H$

and

$$(x, z) = d(\hat{x}, \hat{z}) \tag{14}$$

into (3) we can obtain the linearized nondimensional equations

$$\frac{\partial}{\partial \hat{t}} \hat{\nabla}^2 \hat{\psi}' = \mathrm{Pr\,Ra} \frac{\partial}{\partial \hat{x}} \hat{\theta}' + \mathrm{Pr} \hat{\nabla}^2 \hat{\nabla}^2 \hat{\psi}',$$
$$\frac{\partial}{\partial \hat{t}} \hat{\theta}' = -\frac{d\hat{\bar{\theta}}}{d\hat{z}} \frac{\partial}{\partial \hat{x}} \hat{\psi}' + \hat{\nabla}^2 \hat{\theta}', \tag{15}$$

$$A_Q + \frac{d^2 \hat{\bar{\theta}}}{d\hat{z}^2} = 0, \tag{16}$$

where $\mathrm{Pr} = K_M/K_H$ is the turbulent Prandtl number, $\mathrm{Ra} = (gF_0 d^4)/(\Theta_0 K_H^2 K_M)$ is the Rayleigh number, and $A_Q = \hat{Q}(d/F_0)$ is the nondimensionalized internal forcing, which depends on height. Here $\hat{\ }'$ denotes a nondimensional disturbance with an infinitesimal amplitude. The nondimensional boundary conditions are thus

$$\frac{\partial}{\partial \hat{z}} \hat{\psi} = 0, \quad \hat{\psi} = 0, \quad \text{and}$$
$$\frac{\partial}{\partial \hat{z}} \hat{\theta} = (c_b K_H)/F_0 \quad \text{at} \quad \hat{z} = 0; \tag{17}$$

$$\frac{\partial^2}{\partial \hat{z}^2} \hat{\psi} = 0, \quad \hat{\psi} = 0, \quad \text{and}$$
$$\frac{\partial}{\partial \hat{z}} \hat{\theta} = (c_t K_H)/F_0 \quad \text{at} \quad \hat{z} = 1. \tag{18}$$

Solving (16) by using the boundary conditions for $\hat{\theta}$ given in Eqs. (17) and (18), we obtain

$$-\frac{d\hat{\bar{\theta}}}{d\hat{z}} = \frac{1}{n}(n+1)^{(1+1/n)} \hat{z}(1 - \hat{z}^n), \tag{19}$$

which is height dependent and has a maximum at $\hat{z} = \hat{z}_0$ [see Eq. (10)].

The disturbances can be expanded into a complete set of normal modes:

$$\hat{\psi}' = ie^{\lambda \hat{t}} e^{ik\hat{x}} \Psi(\hat{z}),$$
$$\hat{\theta}' = e^{\lambda \hat{t}} e^{ik\hat{x}} \Theta(\hat{z}), \tag{20}$$

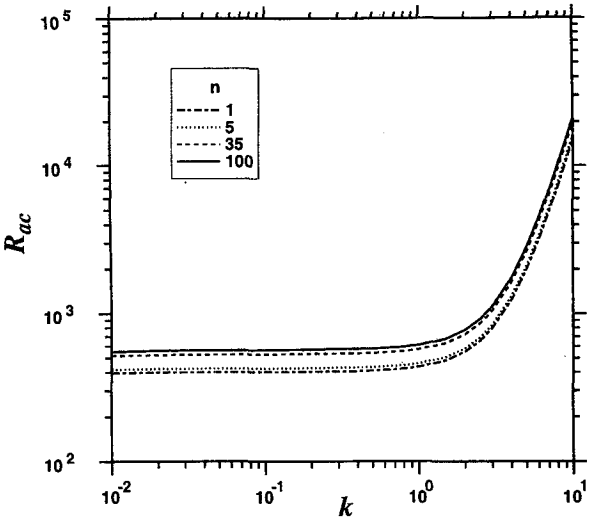

FIG. 3. The dependence of Ra_c on wavenumber, k, with various values of the internal heating–cooling parameter, n.

where λ is a nondimensional growth rate, and k is a nondimensional wavenumber. Substituting (20) into (15) and using the boundary conditions given by (17) and (18), we obtain the following equations:

$$\mathrm{Pr}\,\mathrm{Ra}k\Theta(\hat{z}) + \mathrm{Pr}(D^4 - 2k^2D^2 + k^4)\Psi(\hat{z}) = \lambda(D^2 - k^2)\Psi(\hat{z}),$$

$$(D^2 - k^2)\Theta(\hat{z}) + D\bar{\theta}k\Psi(\hat{z}) = \lambda\Theta(\hat{z}), \quad (21)$$

where $D^m \equiv d^m/d\hat{z}^m$ $(m = 1, 2, 4)$. The boundary conditions derived from (17) and (18) are

$$\Psi|_{\hat{z}=0,1} = 0, \quad D\Psi|_{\hat{z}=0} = 0,$$

$$D^2\Psi|_{\hat{z}=1} = 0, \quad \text{and} \quad D\Theta|_{\hat{z}=0,1} = 0. \quad (22)$$

Here we have used $c_b = c_t = 0$ for the first situation.

Discretizing (21) and (22) gives an eigenvalue problem of the form

$$A(\hat{z}_i, k, \mathrm{Ra})X(\hat{z}_i) = \lambda B(k)X(\hat{z}_i), \quad (23)$$

where the growth rate λ is the eigenvalue, and we assume that $\mathrm{Pr} = 1$. The parameter $\hat{z}_i$ is the discretized nondimensional height, with the subscript i indicating the levels. The discretized form is necessary since (23) has to be solved numerically. The unknowns $\Psi(\hat{z}_i)$ and $\Theta(\hat{z}_i)$ compose the eigenvector $X(\hat{z}_i)$. A critical Rayleigh number corresponds to $\lambda = 0$. Given a value of n, $d\bar{\theta}/d\hat{z}$ is determined using (19). Then Ra_c is determined from (23) for a given k, by adjusting Ra so that the largest $\lambda = 0$.

Figure 3 gives the dependence of the critical Rayleigh number, Ra_c, on the wavenumber, k, and the strength of cloud-top cooling, n, from the linear analysis. Obviously the minimum Ra_c occurs at $k \sim 0$, the longest wave, for all given n. This agrees with Sasaki's (1970) conclusion for the case without internal cooling. It also agrees with Fiedler's (1993) analysis.

The preferred scales of the growing modes are presented in Fig. 4, which shows the change of λ with k for given n and $\mathrm{Ra}/\mathrm{Ra}_c$ $(n, k = 0)$, where Ra_c $(n, k = 0)$ is the critical Rayleigh number at the given n. Note that the solid lines are for $n = 1$, and the dashed lines are for $n = 5$, 35, and 100, respectively. The four lines with different n overlap in Fig. 4b for each $\mathrm{Ra}/\mathrm{Ra}_c$ $(n, k = 0)$. Before we discuss these plots, we need to clarify the subtle difference between the concepts of "linear model" and "linear regime." By linear model we mean that the nonlinear terms associated with advection in Eq. (3) can be approximated by linear terms [Eq. (15)] using a small perturbation method; this is a mathematical concept. By linear regime we mean that Ra is close to Ra_c, so that interactions among waves with different wavenumbers can be ignored; this is a physical concept. Conceptually a linear model could be applied to either a linear ($\mathrm{Ra} \sim \mathrm{Ra}_c$) or a nonlinear ($\mathrm{Ra} \gg \mathrm{Ra}_c$) convective regime as long as the amplitude of

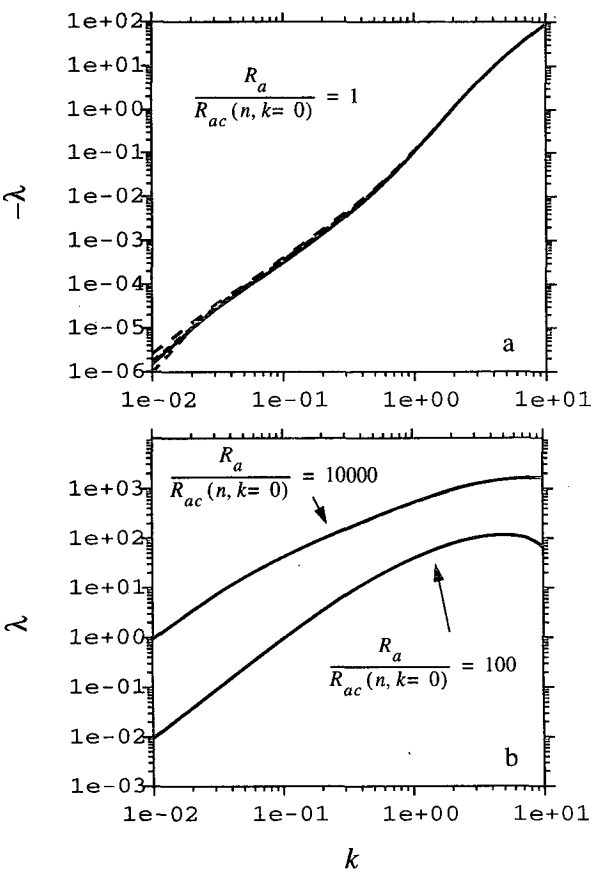

FIG. 4. The dependence of growth rate (λ) on wavenumber k with various internal heating–cooling parameter, n, and different convective regimes: (a) $-\lambda$ for $\mathrm{Ra}/\mathrm{Ra}_c$ $(n, k = 0) = 1$ and $n = 1$, 5, 35, and 100; (b) λ for $\mathrm{Ra}/\mathrm{Ra}_c$ $(n, k = 0) = 100$ and $\mathrm{Ra}/\mathrm{Ra}_c$ $(n, k = 0) = 10\,000$, and $n = 1$, 5, 35, and 100. Note that lines overlap for various n in (b).

the perturbed motion is small, and thus wave–wave interactions can be ignored. However, if the perturbation grows exponentially into the nonlinear regime, so that wave–wave interactions are inevitable, then the linear model becomes inapplicable.

For the linear regime, Fig. 4a shows that the decay rate increases dramatically with k. Note that the ordinate is $-\lambda$, so that a positive value means a decaying mode. The mode $k \sim 0.1$ decays more than 100 times faster than the mode $k \sim 0.01$, although the difference of their critical Rayleigh numbers is relatively small.

In the nonlinear regime, shown in Fig. 4b, the large Ra allows a large range of exponentially growing modes to coexist and interact with each other. For $\mathrm{Ra}/\mathrm{Ra}_c\,(n, k = 0) = 100$, the maximum λ occurs for $k = 5$, whereas for $\mathrm{Ra}/\mathrm{Ra}_c\,(n, k = 0) = 1$ it occurs for $k = 0$. This does not mean, however, that the linear model predicts the dominance of a short mode for $\mathrm{Ra}/\mathrm{Ra}_c\,(n, k = 0) = 100$. The linear model is simply irrelevant to the nonlinear regime after the exponential growth of the modes, although it may apply initially when convection just starts. Figure 4 suggests that to apply the linear model to MCC, which is a quasi-steady phenomenon, only solutions in the linear regime are relevant. The application of weakly nonlinear and fully nonlinear models is discussed in the remainder of this paper.

We conclude from Figs. 3 and 4 that it is not possible to form quasi-steady narrow downdrafts in the linear regime, which must include short-mode components. Thus, although mesoscale circulations are preferred in the linear model with constant boundary conditions, cloud-top cooling cannot produce closed MCC in a linear regime.

Figures 3 and 4 show that the qualitative properties of the solutions are not sensitive to the value of n. The insensitivity of the linear solutions to the cloud-top cooling leads us to conclude that *the linear model is not capable of representing the effects of the cooling on the model dynamics.* The cooling is balanced by diffusion at the first order, as shown in Eq. (16). This conclusion is also supported by Austin's (1995) results, based on a different linear model that includes parameterized moisture effects. He found that the buoyancy production and dissipation are not sensitive to the basic-state stratification generated by cloud-top cooling.

The above conclusions suggest that nonlinear solutions have to be pursued. The nonlinear effects can be first investigated through a weakly nonlinear analysis.

4. Weakly nonlinear analytical solution

By assuming that the aspect ratio of the convective circulations is large, we can analyze the effects of weakly nonlinear processes to see whether or not nonlinear effects can generate closed circulation patterns. To relax the linear approximation, we need to relax the infinitesimal amplitude assumption required by linear theory. For this purpose, a perturbation or small-parameter method is employed following Chapman and Proctor (1980).

The inverse of the aspect ratio of the cell, $\epsilon = H/L$, is identified as the small parameter. The variables in the nondimensionalized equations of (3) are expanded in terms of ϵ. Here H represents the height of the cell, and L represents the width of the cell. Note that H is of the same order as the STBL depth. Thus, the wavenumber of the cells is $k = O(\epsilon)$, as shown in Fig. 5, which is an idealization of Fig. 3. The Rayleigh number related to this wavenumber is $\mathrm{Ra}_c = \mathrm{Ra}_c\,(k = 0) + \mu^2\epsilon^2$ $(0 < \mu^2 \leq 1)$ (Hurle et al. 1967; Sasaki 1970). When $\mu^2 = 1$, $\epsilon^2 = \mathrm{Ra}_c - \mathrm{Ra}_c\,(k = 0)$. Therefore, the solution is slightly supercritical and weakly nonlinear. The value of Ra_c is also indicated in Fig. 5. This small-parameter method has been used by Childress et al. (1975) to study the problem of convection due to swimming microorganisms and by Chapman and Proctor (1980) to study mantle convection. No limit is imposed on the amplitude of the motion.

The derived prognostic equation for potential temperature at the leading order is (Chapman and Proctor 1980; Shao 1994)

$$F_T = -\mu^2 F_{\xi\xi} - F_{\xi\xi\xi\xi} + (F_\xi^3)_\xi - \alpha(F_\xi F_{\xi\xi})_\xi, \quad (24)$$

where F, T, and ξ are, respectively, the transformed nondimensional potential temperature at the leading order, time, and horizontal coordinate. The transformed nondimensional streamfunction is given by $G \propto F_\xi$. Note that the equation is vertically integrated so that the coefficient α represents all the vertically asymmetric effects from $\dot{Q}$ and the boundary condition on the horizontal velocity [Eqs. (4) and (5)]. The last two terms of the equation arise from the nonlinear advection.

The changes of G and F with α at steady state, for $\mu^2 = 1$, are shown in Fig. 6. The cell is symmetric for

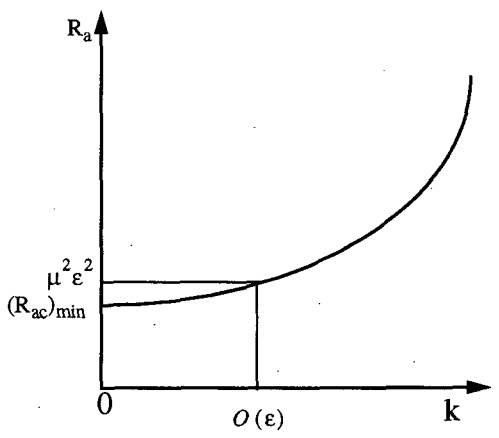

FIG. 5. A schematic illustration of the relation between Ra_c and k from linear theory. The minimum Ra_c is $\mathrm{Ra}_c\,(k = 0)$.

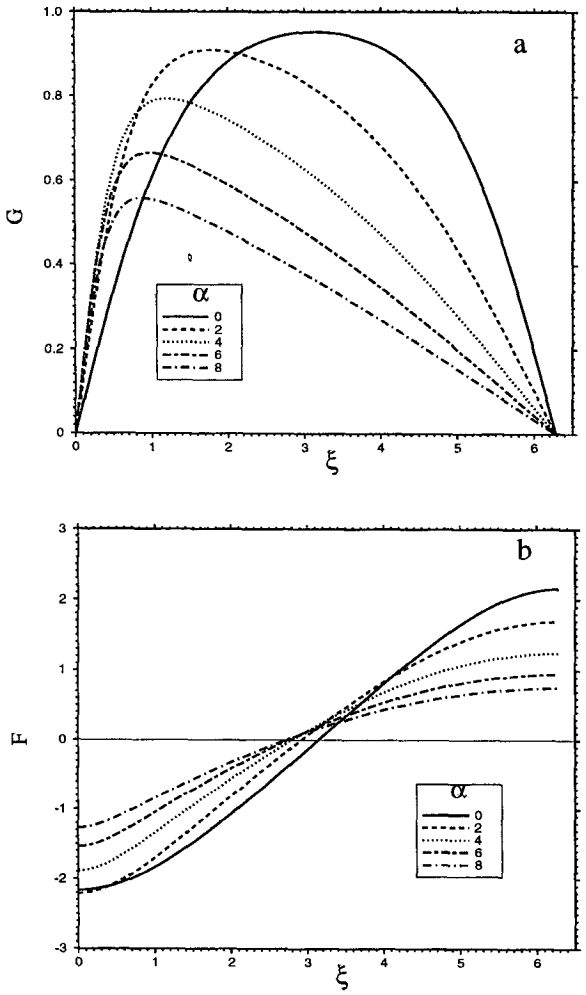

FIG. 6. The solution for (a) streamfunction G and (b) potential temperature F as a function of α.

$\alpha = 0$ and asymmetric for $\alpha > 0$. Obviously the larger α is, the more asymmetric the flow structure is. The immediate questions are how α changes with n (interpreted as a measure of the strength of the cloud-top cooling), and how large it can be for a typical STBL. For the three situations discussed in section 2, and with $F_0 = 0.23$ K m s^{-1}, the dependences of Ra_c ($k = 0$) and α on n are shown by the solid lines in Figs. 7a and 7b, respectively, for the first situation when only internal heating/cooling exists and by the dashed lines for the third situation when both internal heating/cooling and boundary fluxes exist. For the second situation, that is, only boundary fluxes exist, Ra_c ($k = 0$) = 320 and $\alpha = 0.853$.

Figure 7 shows that α increases with n, or the strength of the cloud-top cooling. However, α approaches an asymptotic value of 1.3 (solid line) and 1.0 (dashed line) in Fig. 7b, which suggests that the circulation pattern can only be intermediate between those for $\alpha = 0$ and $\alpha = 2$ as shown in Fig. 6. We conclude that *the effect of cloud-top cooling on the model dynamics does show up in the weakly nonlinear analysis.* This effect is limited, however, since α approaches small asymptotic values as the cloud-top cooling becomes stronger.

The positive α for the second situation indicates that the vertically asymmetric dynamical boundary conditions for horizontal velocity also help generate closed circulation patterns. It implies that a free-slip upper boundary may allow stronger horizontal advection at the top than the nonslip lower boundary at the bottom and thus may prefer narrower but stronger downdrafts.

The importance of nonlinear processes to the above results is obviously suggested by Eq. (24). If there were no nonlinear processes, the last two terms in the equation would be zero. The solution would be like the one with $\alpha = 0$ in Fig. 6, and thus there would be no

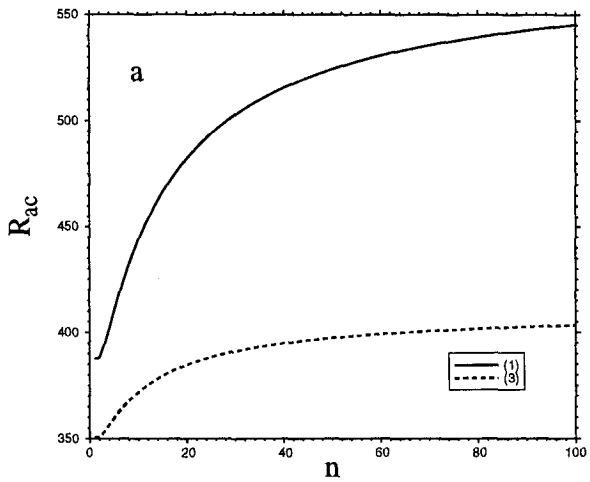

FIG. 7. The change of Ra_c and α with n for the first situation (1) and third situation (3).

asymmetric circulations. This is consistent with our linear analysis, which showed that the effects of cloud-top radiative cooling cannot be represented in a linear model.

The main deficiency of the weakly nonlinear model is that it requires strong diffusion. As discussed earlier, under the weakly nonlinear assumption the motions are slightly supercritical, and Ra_c is slightly larger than Ra_c ($k = 0$). For the cases we are studying (Fig. 7), the range of Ra_c is about 320 to 510. For a given heating/cooling profile (or F_0) and layer depth, the only mechanism that can force Ra_c to be close to Ra_c ($k = 0$) is diffusion. This can be seen from the definition of Ra:

$$\mathrm{Ra} = (gF_0d^4)/(\Theta_0K_H^2K_M). \tag{25}$$

Let us use $F_0 = 0.23$ K m s^{-1}, $d = 1500$ m, and take $g = 9.8$ m s^{-2}, $\Theta_0 = 300$ K, and Ra = 500. Then (25) gives $K_H = K_M = 424$ m^2 s^{-1} for Pr = 1. Those values are at least an order of magnitude larger than the diffusion coefficients usually applied for a convective STBL. The strong diffusion balances out the forcing at leading order. If we take $K_H = K_M = 30$ m^2 s^{-1}, as is more appropriate for a STBL (Krishnamurti 1975; Van der Borght and Agee 1978; Helfand and Kalnay 1983; Chlond 1988), then Ra is 1.5×10^6, which is much larger than Ra_c. This would imply that nonlinear processes should be fully expressed by the model and thus leads us to search for fully nonlinear solutions.

A further interesting point is that although the linear analysis in the last section and the weakly nonlinear analysis in this section are for the 2D (x–z) model [Eq. (3)], the conclusions from these analyses will not change qualitatively when a second horizontal dimension (y) is added to the model as long as the boundary condition in y-direction is also periodic. The y-component will be parallel to the x-component in the linear analysis, and it does not affect the value of α at all in the weakly nonlinear analysis. So the conclusions of these two sections can be generalized for the 3D case. Specifically, *cloud-top radiative cooling can generate closed MCC in a nonlinear model, no matter whether the model is* 2D *or* 3D. It supports the relevance of our 2D model for this study.

5. Nonlinear numerical solutions

a. Numerical schemes and model parameters

The fully nonlinear form of (3) has to be solved numerically. We employ an Arakawa C grid to stagger the variables, the Takacs (1985) scheme for θ-advection, the Arakawa Jacobian (Arakawa 1966) for ζ-advection, and the third-order Adams–Bashforth scheme (Durran 1991) for time differencing. The multigrid method (Brandt 1977) is used to solve the Poisson equation for the steamfunction.

The five cases listed in Table 1 have been simulated. The domain size is 32 km horizontally and 1.5 km vertically. Larger domains are discussed later. The diffusion coefficients are $K_H = K_M = 30$ m^2 s^{-1}, so that Pr = 1. This value of the diffusion coefficient is typical for the marine boundary layer and has been used in previous studies such as Krishnamurti (1975), Van der Borght and Agee (1978), Helfand and Kalnay (1983), and Chlond (1988) for the study of shallow mesoscale circulations. The above parameters give Ra = 1.44×10^6, which corresponds to $\mathrm{Ra}/\mathrm{Ra}_c \sim 10^3$, based on $Ra_c \sim 500$ as shown in Fig. 3. This value of Ra agrees with the observed value, as given by Krishnamurti (1975). The cases are run with $\Delta x = 250$ m, $\Delta z = 30$ m, corresponding to 130×50 grid points, and with $\Delta t = 0.5$ s. Each case is perturbed initially with the same random perturbation of potential temperature, with an amplitude of 0.05 K, and is run for 24 simulated hours.

b. Steady-state solutions

1) CELL SCALES AND PATTERNS

All of the simulations reach a steady state after about 20 simulated hours. Figure 8 shows the distributions of the streamfunctions at the end of the 24th hour for the five cases shown in Fig. 2. Obviously mesoscale cells appear for case 1 when cloud-top cooling is concentrated at the top ($n = 35$) (Fig. 8a). As n changes from 35 to 1 (Figs. 8a–c), the number of cells in the domain changes from two to ten. By observing Figs. 8a–c, the decrease of cell size with n is due to the decrease of the width of updrafts, while the width of downdrafts remains about the same. The strength of updrafts ($w = \partial\psi/\partial x$) is much weaker than that of the downdrafts for cases 1 and 2. Figure 8d for case 4 ($n = 0$) shows that constant fluxes at the boundaries cannot generate mesoscale cells without concentrated cloud-top cooling. Figure 8e for case 5 shows that mesoscale cells tend to appear when both constant heat fluxes at the boundaries and cloud-top cooling exist.

The above results suggest that *nonlinear processes are crucial for determining the effects of cloud-top cooling on the model dynamics and hence the scales of the circulation.* Stronger cloud-top cooling is associated with wider updrafts and thus larger cells. In contrast, the constant-flux boundary condition by itself cannot maintain a mesoscale circulation in the fully nonlinear regime (case 4). Our results further suggest that a linear theory can tell us what wavenumber appears most easily or grows fastest at the onset of convection (Figs. 3 and 4), but not what wavenumber will dominate when convection is fully developed. When the Rayleigh number is very large ($\mathrm{Ra}/\mathrm{Ra}_c \gg 1$) so that motions on all scales can occur, there is no obvious reason to believe that either $k \sim 0$ or a larger k (Fig. 4) should appear and dominate. Mechanisms like cloud-top cooling must be there to "select" the mesoscale cells.

Figure 9 shows the potential temperature distributions. The common feature of the potential temperature

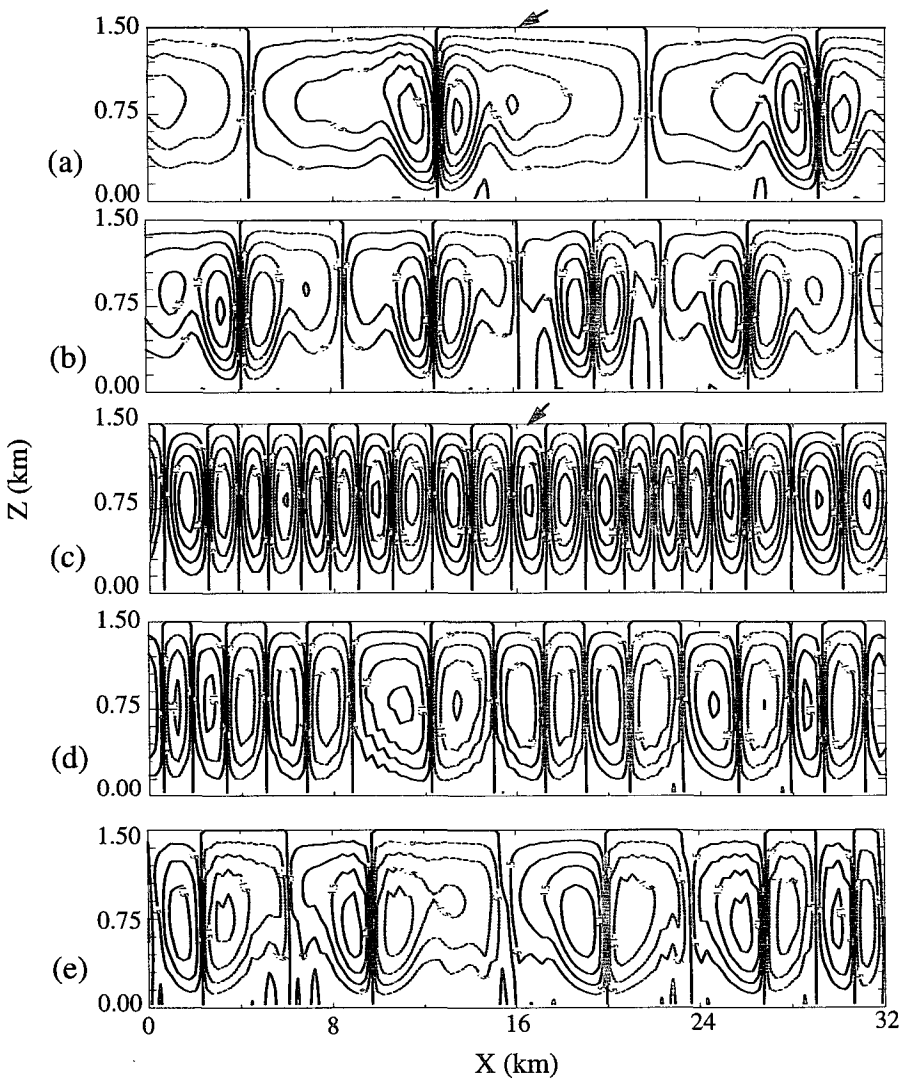

FIG. 8. Streamfunctions at the end of the 24th hour for the five cases listed in Table 1. The unit is 10^3 m^2 s^{-1}. The contour interval is 0.25×10^3 m^2 s^{-1}.

structures for the five cases is that cold cores are associated with downdrafts and warm cores with updrafts, except near the very top and bottom, where the motions are essentially horizontal (see Fig. 8). Midlevel inversions exist in cases 1, 2, and 5 (Figs. 9a, 9b and 9e), that is, the cases in which mesoscale circulations occur, obviously due partly to the spreading out of warm air from the warm cores at the upper levels and the "splashing" of cold air from the cold cores at the lower levels. Moreover, small-scale warm cores appear on the sides of each downdraft for these cases, and are about the same size as the small-scale circulations in cases 3 and 4 (Figs. 9c, 9d). This "two scale" structure, which appears only when cloud-top cooling is present, may indicate that the cooling helps parcels to "escape" from the small-scale circulations to form mesoscale circulations.

Since the drastic differences of cell shape and potential temperature distributions between cases 1 and 3 are due only to the changes of the cloud-top cooling, we choose these two cases for further analysis. Figure 10 shows the coherent structures of potential temperature and vertical velocity at the middle level of the domain for case 1 (Fig. 10a) and case 3 (Fig. 10b). The motions in these two cases are driven by buoyancy at the cores of the updrafts and downdrafts. In between the cores, however, gravity waves exist for case 1 due to the existence of the midlevel inversion (Fig. 9). The suppression of convection by this inversion plays a crucial role in the formation of

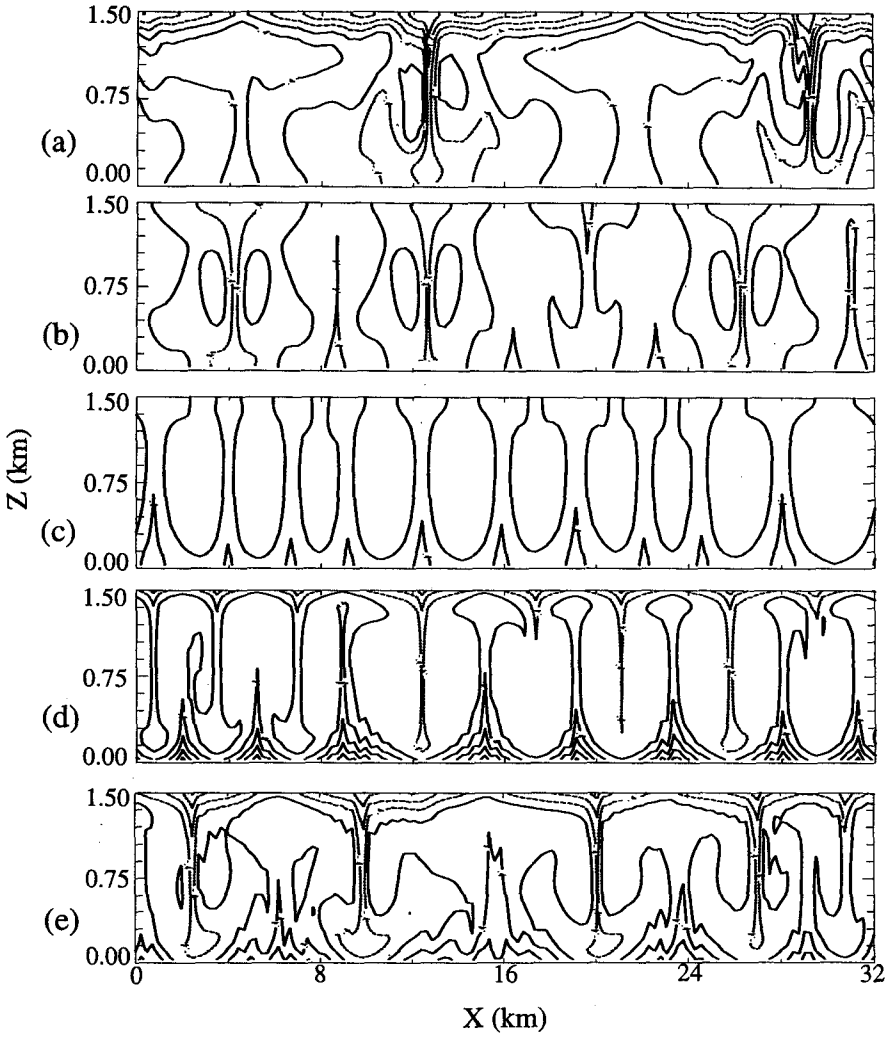

FIG. 9. The same as Fig. 8 except for the potential temperature. The contour interval is 0.4 K.

mesoscale circulations, as shown by the later trajectory analysis.

Another interesting point from Fig. 10 is that although the updrafts are wide for case 1, the vertical motion is concentrated in the very narrow centers of the updrafts, while the upward motion around the centers is very wide but mild. This agrees with our expectation that weak mesoscale updrafts exist to support the existence of mesoscale cloud patches in closed MCC.

2) DISCUSSION

Because we have used a simple 2D model, questions may be raised regarding the reasons for the occurrence of the mesoscale circulations in case 1. Are they due to the cloud-top radiative cooling or to a 2D energy anticascade? How do they depend on the diffusion coefficient, or Ra? Is the domain size a limitation?

Cloud-top radiative cooling is definitely a contributor to the formation of closed MCC, in either 2D or 3D, as we concluded from our analyses in the previous two sections. But there is no doubt that a 2D energy anticascade exists in all 2D models. The question now is which process, the cloud-top radiative cooling or the 2D energy anticascade, contributes more directly to the formation of the mesoscale circulations.

The energy anticascade process in a 2D viscous dynamical model was simulated by Lilly (1969). In his study, a prescribed monochromatic forcing at k_e (the wavenumber of the energy-containing eddies) drives the motions, so that the spectrum of turbulent kinetic energy follows $k^{-5/3}$ when $k < k_e$, and k^{-3} when $k > k_e$, as predicted by Kraichnan (1967). This cascade is shown schematically by the solid line in Fig. 11.

Figure 12 shows the spectra of TKE (Figs. 12a and 12b) and enstrophy (Figs. 12c and 12d) at the middle

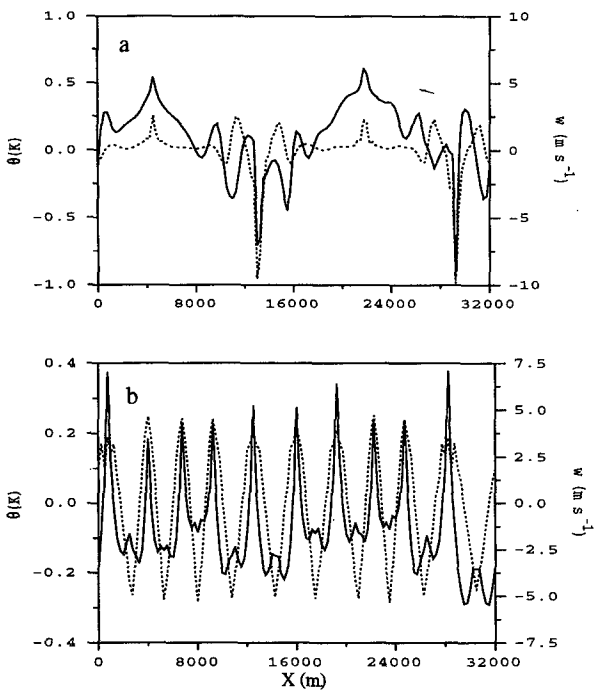

FIG. 10. The coherent structure of potential temperature (solid lines) and vertical velocity (dashed lines) at the middle level of the domain for (a) case 1 and (b) case 3.

level for cases 1 and 3, respectively. The three lines in each panel represent the spectra at the end of the 22nd, 23rd, and 24th simulation hours, respectively, and their consistency indicates that the spectra are representative of the flow features. Note that only the range with $k \leq 32$ (wavelength $\geq 4\Delta x$) is meaningful in this discussion due to the existence of aliasing and truncation errors in the model. Obviously neither the $-5/3$ nor the -3 law fits the slopes of the profiles. However, since the solutions have reached a steady state, turbulence should have become fully developed and should follow the slopes as predicted. What is the explanation?

Comparing our 2D dynamical model with that of Lilly (1969), the only difference comes from the driving force. The domain-integrated steady-state kinetic energy (KE) equation, corresponding to our vorticity equation, is

$$\frac{g}{\Theta_0}\langle w\theta\rangle = \langle K_M\zeta^2\rangle, \tag{26}$$

where $\langle\ \rangle$ denotes domain integration. This shows that the KE, as converted from the potential energy (PE) by $(g/\Theta_0)\langle w\theta\rangle$ (>0), is dispersed upscale by $\langle K_M\zeta^2\rangle$ as an anticascade process. The forcing related to the conversion is the buoyancy term, $(g/\Theta_0)(\partial\theta/\partial x)$. If $(g/\Theta_0)(\partial\theta/\partial x)$ were monochromatic, as assumed by Lilly (1969), there is no doubt that the $-5/3$ and -3 slopes would appear, since we end up with the same dynamical equation. However, in our model $(g/\Theta_0)(\partial\theta/\partial x)$ is determined by the model itself, that is, by the thermodynamics of the model, as given by the prescribed cloud-top cooling, $\dot{Q}$. This self-determined forcing of the dynamics cannot be monochromatic but is polychromatic, as shown in Fig. 13, which shows the spectrum of $(g/\Theta_0)(\partial\theta/\partial x)$ at the midlevel of the domain for cases 1 and 3.

For case 1 there are two dominant peaks. One is for the mesoscale and the other is for the small scale. A polychromatic forcing can complicate the 2D energy spectrum. This can be demonstrated schematically by the two spectra that are driven respectively by different monochromatic forcings at k_e and k_{e1}, as shown in Fig. 11. If there is no energy sink between k_e and k_{e1}, as in our model, the slope of the sum of the two spectra would follow neither $-5/3$ nor -3. Similarly, simulations by Zeng and Pielke (1993) using a more complicated 2D model with a one-wave driving force due to land–water contrast obtained no obvious $-5/3$ or -3 slopes in their spectra because of self-determined polychromatic forcing that arises through the dynamics and thermodynamics of their model.

Since the peaks in Figs. 12 and 13 are closely correlated, we conclude that the dynamical forcing plays a more direct role than upscale energy cascade in forming mesoscale circulations of case 1. Due to the coexistence of dynamics and thermodynamics in our model, the mesoscale components of the dynamical forcing and the circulations can interact.

As to the diffusion, it is reasonable to expect that our results are sensitive to the diffusion coefficients. We first consider how diffusion affects the conversion of PE to KE. Following Helfand and Kalnay (1983), the domain-integrated PE equation can be written as

$$\frac{g}{\Theta_0}\langle w\theta\rangle = -\frac{g}{\Theta_0}L\int_0^d \dot{Q}z\,dz + \frac{g}{\Theta_0}LK_H[\theta(d) - \theta(0)], \tag{27}$$

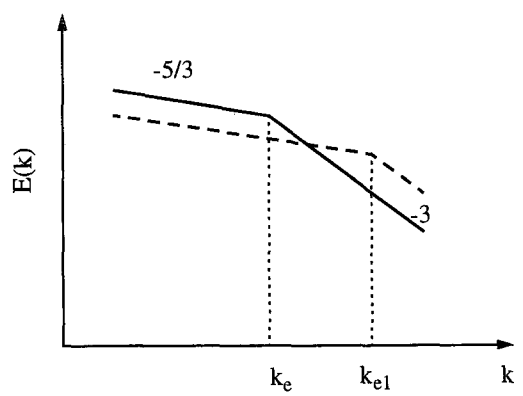

FIG. 11. A schematic description of the $-5/3$ and -3 laws for the two energy spectra with the input of energy from wavenumbers k_e (solid) and k_{e1} (dashed), respectively.

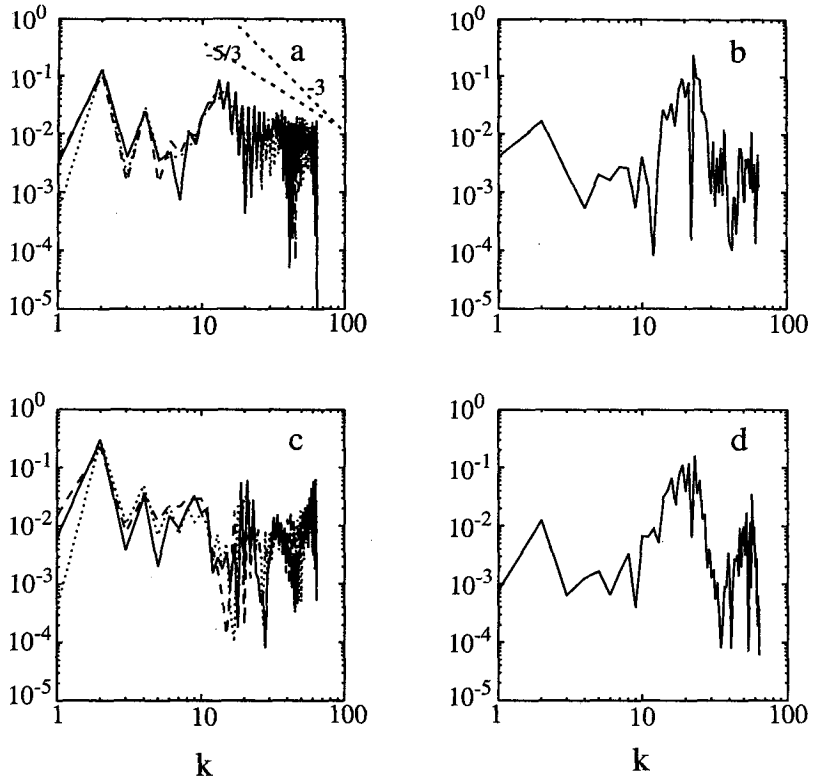

FIG. 12. Power spectrum of kinetic energy [(a) and (b)] and enstrophy [(c) and (d)] for cases 1 and 3, respectively, at the middle level of the domain. Note the three lines for case 3 are overlapped.

where L is the horizontal domain size. Since $[\theta(d) - \theta(0)] < 0$ for a given cloud-top cooling, $\dot{Q}$, a larger K_H will result in a smaller $(g/\Theta_0)\langle w\theta\rangle$, and thus less KE. When the diffusion coefficient is extremely large, so that the convection simulated by the model occupies a quasi-linear or weakly nonlinear regime, the two terms on the right-hand side are nearly in balance, and the effects of cloud-top cooling on the model dynamics are weak. This agrees with what we concluded in the previous two sections.

Several sensitivity simulations have been done to investigate the effects of diffusion on the cell sizes. Results (not shown here) show that three cells appear when the diffusion coefficients are changed from 30 to

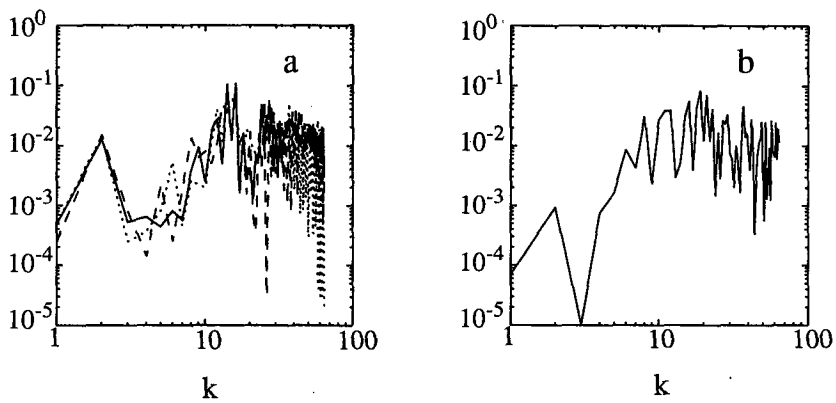

FIG. 13. The energy spectrum of $(g/\Theta_0)(\partial\theta/\partial x)$ at the midlevel of the domain for cases 1 (a) and 3 (b). Note the three lines for case 3 are overlapped.

50 $m^2 s^{-1}$, or Ra is reduced by one-half of an order of magnitude. A two-cell structure still tends to appear at the end of the integration (24 hours) when the vertical diffusion coefficient is kept at 30 $m^2 s^{-1}$, while the horizontal diffusion coefficient is changed from 30 to 100 $m^2 s^{-1}$. Thus, the results appear to be more sensitive to the vertical diffusion coefficient than to the horizontal diffusion coefficient. This is not surprising since the basic forcing $\dot{Q}$ is only vertically asymmetric. Actually, with the periodic lateral boundary conditions, the horizontal diffusion does not appear in Eq. (27) at all. Thus mesoscale circulations can occur in our model with a reasonable range of the values of diffusion coefficients.

The cell sizes and patterns are not sensitive to the horizontal domain size. By increasing the domain size from 32 km of case 1 to 64 and 128 km, respectively, the number of cells in the domain increases correspondingly, as shown in Fig. 14 (see Fig. 15a for case 1) by the vertical velocity at the midlevel of the domain. Although the number of cells does not exactly double with a doubling of the domain size, similar mesoscale structures exist in all the cases.

c. *Evolution of the cells in cases 1 and 3*

1) THE EVOLUTION OF THE CELL SIZES

Figure 15 shows the time evolution of the vertical velocities at the middle level of the domain, that is, 750 m, for cases 1 (Fig. 15a) and 3 (Fig. 15b). We count the number of cells by the number of downdrafts or the number of regions indicated by $w < 0$ (dashed lines). In case 1, after the initial random perturbation, the number of cells changes from 10 to 5 at about the 4th simulation hour, to 3 at about the 10th hour, and to 2 at about the 17th hour. This timescale for mesoscale circulations to develop seems reasonable and agrees with

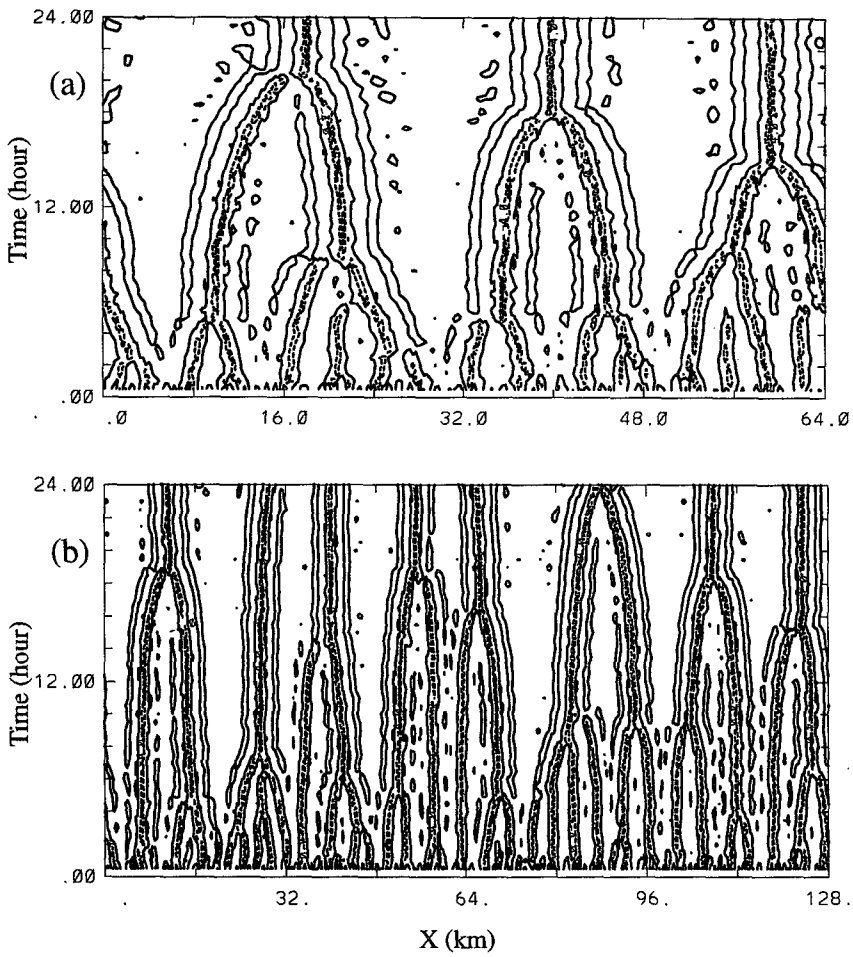

FIG. 14. The sensitivity tests of the horizontal domain size for case 1: (a) 64 km and (b) 128 km. The quantity shown is the vertical velocity at the middle level of the domain with the contour interval of 4 m s^{-1}. Dashed lines show negative values.

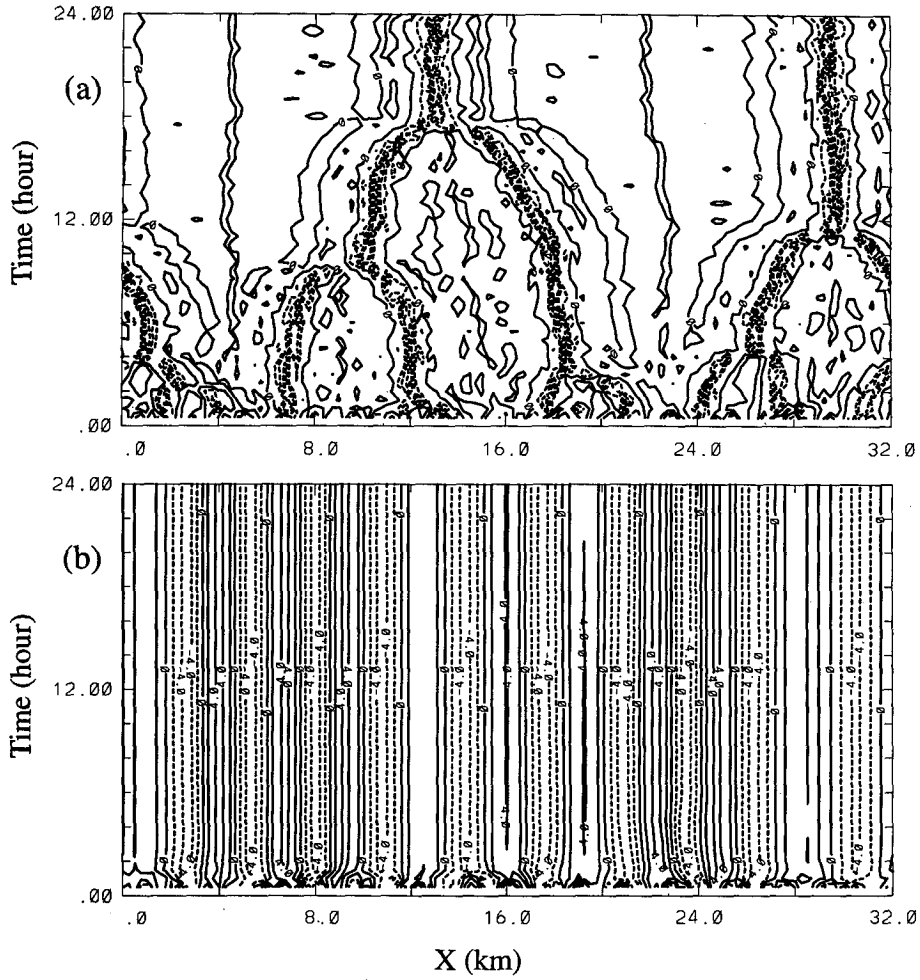

FIG. 15. Evolution of vertical velocity at the midlevel of the domain for cases 1 (a) and 3 (b). Dashed lines show negative values. The contour interval is 4 m s^{-1}.

that obtained by Sykes et al. (1988) for the evolution of cloud streets. In contrast, in case 3 the number of cells remains steady at ten after the first hour. The different evolutions of the two cases further demonstrate that the cloud-top cooling drives the mesoscale circulations in the model.

2) TRAJECTORY ANALYSIS

Trajectory analyses are used to further trace down the circulations related to the "two scale" structure. A passive parcel is "placed" at the center of the domain (x = 16 km and z = 750 m) at the beginning of the 22nd hour. It is then advected by the resolved vertical and horizontal wind. Its trajectory, cooling rate, and potential temperature are recorded until the end of the experiment at the end of the 24th hour. Figures 16 and 17 show the results for cases 1 and 3, respectively. The circulations corresponding to these trajectories are indicated by the arrows in Figs. 8a and 8c, respectively. The trajectory in Fig. 16a includes one mesoscale cell and two small-scale cells, as shown by the streamfunction in Fig. 8a. The parcel moves counterclockwise and experiences heating or cooling depending on its height (Figs. 16b and 16d). The dashed line in Fig. 16c represents the potential temperature of the parcel during this process, and the solid line represents the potential temperature that the parcel would have had if it had experienced only internal heating–cooling (Fig. 16d). The difference between these two lines represents the effects of diffusion. The parcel escapes from its original small cell to join another small cell near the downdraft, due to a slight increase of potential temperature. It is then cooled near the top of the layer until it is cold enough to join the downdraft. When it reaches the bottom of the layer, it is colder than the air in the warm core and moves upward along the direction of the small cell. Although it is gradually warmed in the lower part of the layer, the air above it is so stable (because of the warm core) that it cannot break through, and it de-

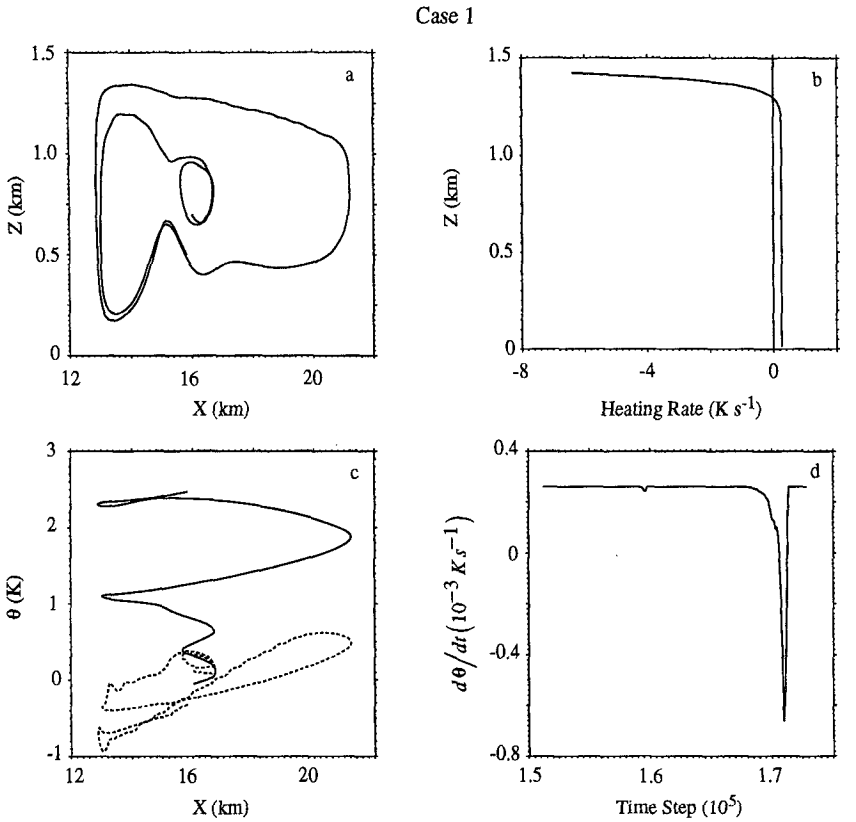

FIG. 16. Trajectory analysis for case 1: (a) trajectory; (b) $\dot{Q}$; (c) solid line—the potential temperature that the parcel would have if only $\dot{Q}$ is considered; dashed line—the parcel's real potential temperature; (d) the instantaneous value of $\dot{Q}$ at the parcel's position.

scends as part of the local downward motion. As shown by Fig. 10, gravity waves also make the parcel move up and down during this period. It finally rises when it has gained enough buoyancy through low-level warming. During this time it has moved horizontally a mesoscale distance. After it shoots up to the top of the layer, where the cloud-top cooling is strong, it slowly sinks back and continues to participate in the mesoscale circulation. In this way, its motion is constrained by the local stable layer, as will be discussed further in next section in terms of heat fluxes, and a mesoscale circulation is formed.

Figure 17 shows the corresponding trajectory and cooling rate for case 3. No mesoscale cells appear in this case (Fig. 17a). This is because the heating/cooling rate is symmetric ($n = 1$) so that the parcel cooled at the top can be warmed up at the bottom at the same rate (Figs. 17b, 17c, and 17d), and thus there is no chance for another scale to develop.

The above trajectory analysis helps explain why more strongly concentrated cloud-top cooling is associated with broader cells. A parcel cooled more strongly at the top of the layer can penetrate readily to the bottom of the layer and takes a longer time to regain its buoyancy. Because it takes longer to warm up, it can move farther horizontally during this warming process, and so it forms a larger cell.

Observations presented by Rothermel and Agee (1980) show that cold parcels emerging from the downdrafts at the lower level are gradually warmed as they move toward the cell center. The data show that the air–sea temperature difference 100 m above the sea surface changes across a closed cell, so that the air temperature is colder than the SST near the downdrafts and warmer than the SST at the cell center. A similar "divergence buoyancy" mechanism was also suggested by Beniston (1985) from his 3D mesoscale simulations of open cells.

d. Nonlinear processes

The trajectory analysis reveals that the circulations are closely related to the structure of potential temperature or the efficiency of the conversion of PE to KE. Convection is suppressed by stable stratification and generated by unstable stratification. As shown by the potential temperature structures in Fig. 9, although convection in these cases is fully developed and reaches a

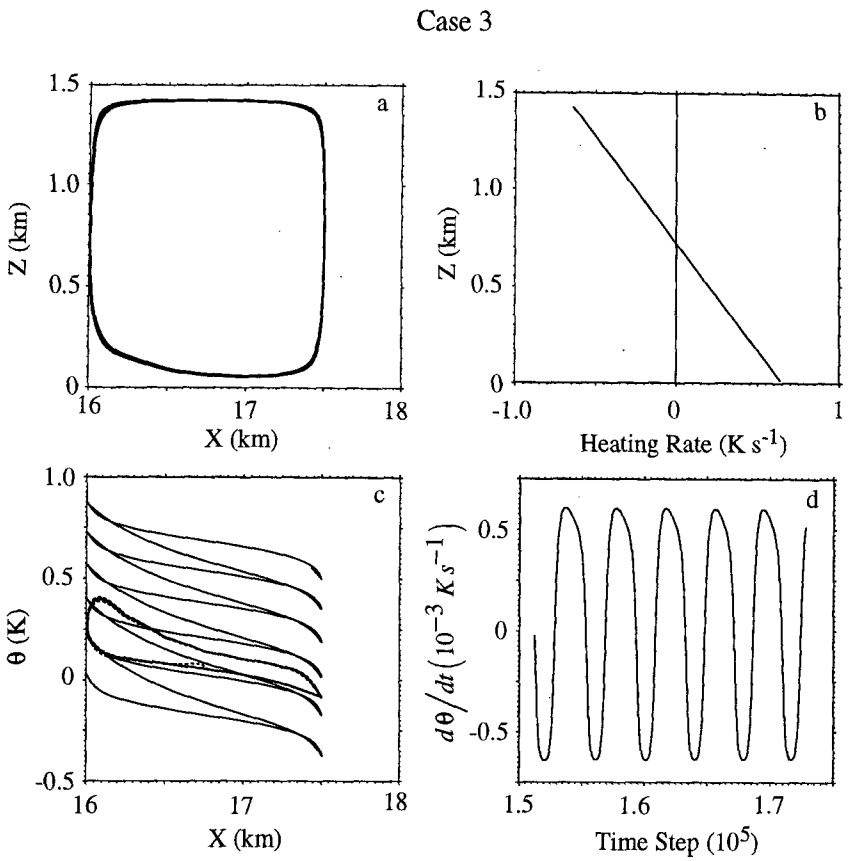

FIG. 17. The same as Fig. 16 except for case 3.

statistically steady state, the potential temperature in the layer is far from well mixed. This is again shown by the horizontally averaged vertical distributions of potential temperature for cases 1 and 3 in Fig. 18. The vertical distributions of potential temperature, averaged for updrafts and downdrafts, respectively, are also shown. In contrast to the monotonic decrease of potential temperature with height in the linear and weakly nonlinear analyses [e.g., Eq. (19)], a nonmonotonic distribution of potential temperature, including a statically stable layer, exists for these fully nonlinear cases. Stable layers exist in both updrafts and downdrafts, but their heights and depths differ between updrafts and downdrafts, as well as from case to case. The stable layer is deep and strong in case 1, where the cloud-top cooling is concentrated at the top, and is shallow and weak in case 3, where the internal heating–cooling is symmetric. Unstable layers exist both above and below the stable layer for case 1, while the stable layer extends to the top in case 3 so that there is no turbulent source at the top.

The fact that the stable layer does not exist in the linear and weakly nonlinear models leads us to conclude that nonlinear processes are necessary to generate and maintain it. The two processes that determine the vertical distribution of potential temperature are the internal heating–cooling and the vertical transport of heat by the motion and by diffusion. The heating–cooling profiles for both cases have cooling in the upper part and warming in the lower part. This heating–cooling by itself would tend to produce a monotonic decrease of potential temperature with height and thus cannot directly cause the stable layer. The vertical transport of heat, on the other hand, includes the parameterized subgrid flux, the small-scale flux, and the mesoscale flux calculated from the filtered vertical velocity and potential temperature, as shown in Fig. 19. The filter used to select mesoscale contributions is given in the appendix, through which the waves with wavenumbers larger than six are greatly damped. The subgrid flux is parameterized as a linear downgradient transport, and hence tends to smooth out the temperature rather than build up a stable layer. The resolved heat flux, in contrast, produces countergradient transports in the stable layer (positive when the subgrid flux is negative), which enhances the stable stratification. This resolved heat flux is positive throughout the layer, converts PE to KE, and maintains the stable stratification through circulations. The stronger the stable layer is, the larger the mesoscale heat flux. Obviously this

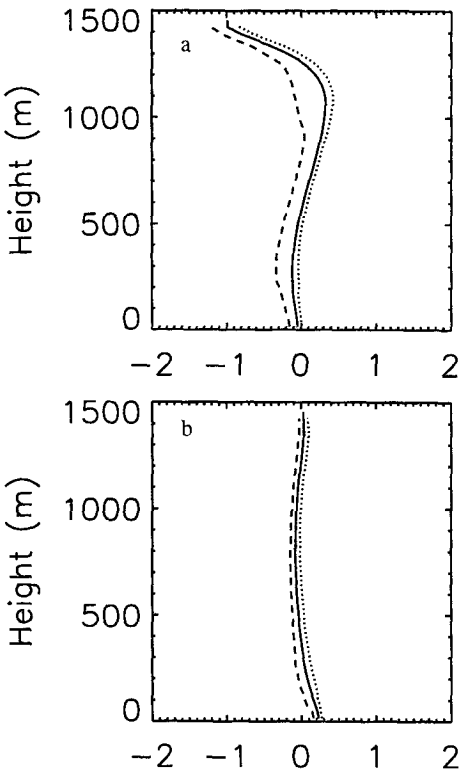

FIG. 18. Horizontally averaged potential temperature profile (solid line), as well as that for updrafts (dotted line) and downdrafts (dashed line) for (a) case 1 and (b) case 3.

stable layer is related to the midlevel inversion as shown in Fig. 9.

The nonlinear effects and their relation to the mesoscale circulations can be further revealed by the distribution of mesoscale potential temperature advection ($K\ s^{-1}$), as shown in Fig. 20 for case 1. The upper and lower panels are for the mesoscale horizontal and vertical advection, respectively. The mesoscale contributions are very distinctive. There is warm horizontal advection near the top (Fig. 20a), which is located at both sides of the cold cores and tends to build up the temperature gradient as well as enhances negative buoyancy at the top of the cold cores. The vertical advection (Fig. 20b) has the same sign as the horizontal advection. In the upper part, it advects warm air where warm horizontal advection occurs, and also advects cold air inside the core. Thus, the total mesoscale advection enhances the horizontal temperature gradient, or negative buoyancy, at the top where the cold cores are rooted, and destabilizes the stratification inside the cores. In short, it supplies cold air to the tops of the downdrafts. Therefore, mesoscale advection enhances the strength of the downdrafts, which in turn provide energy to generate updrafts. Once a mesoscale circulation is initiated as we discussed in the trajectory analysis, it will strengthen itself by enhancing the strength of the downdrafts until a steady state is reached.

e. A conceptual model

The above analyses suggest that two factors are essential for generating and maintaining mesoscale circulations in our model: one is the cloud-top cooling that can constantly generate small-scale convection; the other is a stable layer that helps support the mesoscale circulations. Figure 21 shows a conceptual model based on the above results. Small-scale downdrafts rooted at the top bring cold air from the top to the bottom, after which the cold air moves both vertically and horizontally. In the lower part of the layer, the cold air is warmed up by surface heating, internal heating, or diffusion. The less cold parcels in this cold air may gain buoyancy in a short time and flow into other small-scale cells. However, extremely cold parcels need a longer time to warm up so that they can finally penetrate through the stable layer. During the time they are warming, they may move up slightly and temporarily, but they are pushed down again when they encounter the stable layer. In this way, small-scale convection carries heat into the weak inversion layer and helps to maintain it. The parcels remain in quasi-horizontal motion, however, so that when they are finally warm

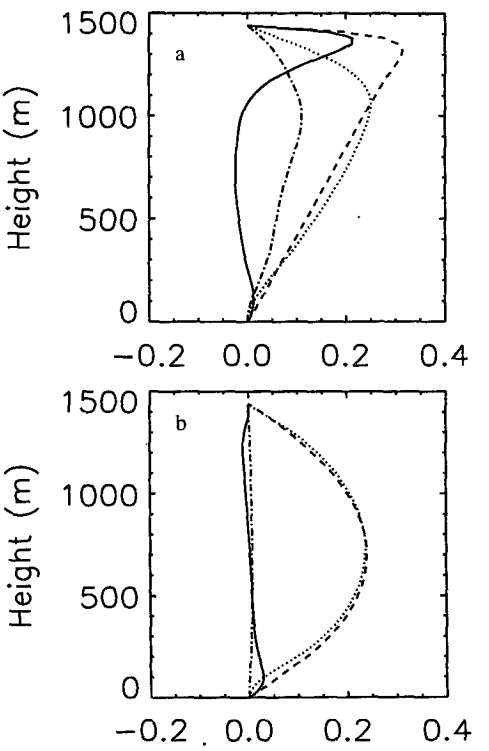

FIG. 19. The horizontally averaged total (dashed line), resolvable (dotted line), mesoscale (dash–dotted line), and subgrid (solid line) heat fluxes ($K\ m\ s^{-1}$) for case 1 (a) and case 3 (b).

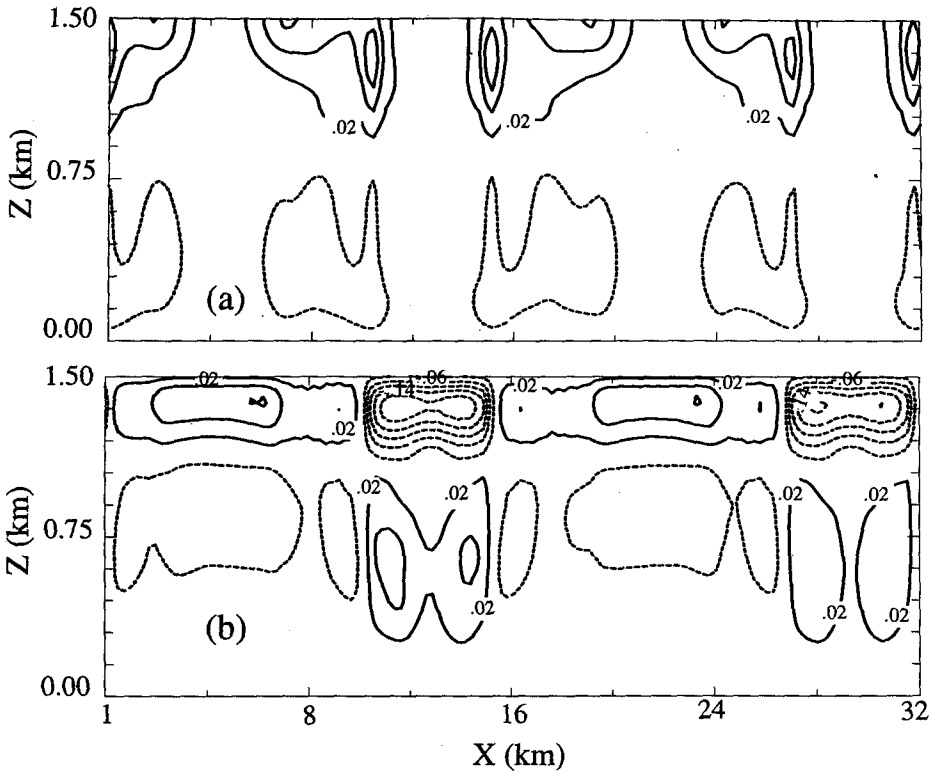

FIG. 20. Mesoscale horizontal (a) and vertical (b) advection of potential temperature for case 1. The contour interval is 0.04 K s^{-1}.

enough to rise through the stable layer, they have moved a mesoscale distance horizontally. In this way, mesoscale convection is generated. Near cloud top, cold parcels transported by the mesoscale circulation may join small-scale circulations at anytime when they have enough negative buoyancy to sink. On the other hand, warm parcels from the updrafts of small-scale cells may also join the mesoscale advection near cloud top at any time and experience cloud-top cooling. Statistically, in a Reynolds-averaged sense, mesoscale advection near cloud top carries cold parcels to downdrafts, which generate kinetic energy for both small-scale and mesoscale circulations, leading to closed MCC. Obviously the cloud-top cooling and the nonlinear processes are two important factors in our model.

Our conceptual model may be applicable to the atmosphere over cold ocean surfaces. The two basic requirements for this mechanism to work are concentrated cloud-top cooling, which is required to generate turbulence near cloud top, and a stable layer in the middle of a STBL, which suppresses vertical motion of small eddies. Cloud-top cooling may be produced by radiative cooling and evaporative cooling, and the stable layer may be the weak cloud-base stable layer that is associated with dynamics, solar heating, and drizzle or the stably stratified trade wind cumulus layer that is

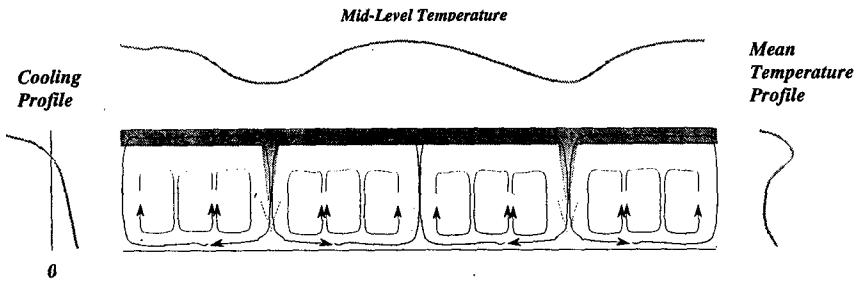

FIG. 21. A conceptual model of closed MCC.

sometimes capped by stratiform cloud (Kropfli and Orr 1993). These various features are frequently observed in the STBL (e.g., Nicholls and Leighton 1986). Rand (1995) also suggested that a cloud-base inversion layer is necessary for generating MCC.

Moreover, our model agrees with observations in some other respects. 1) Mesoscale cloud patches contain small-scale structures (Krueger and Fritz 1961; Hubert 1966). The coexistence of small-scale and mesoscale convection in our model allows both to appear. 2) Closed MCC is observed over both cold and warm water, but it appears more frequently over cold water (e.g., Agee 1987). Cold water adds in the development of closed MCC since it takes a longer time for cold parcels near surface to gain buoyancy. A warm surface may not destroy closed MCC as long as it is not so warm as to regenerate the positive buoyancy of very cold parcels in a very short time or over a very short distance. The simplicity of our model prevents us from quantitatively comparing our numerical results with the observed properties of a STBL. However, the qualitative agreement of our model with observations is encouraging.

6. Conclusions

Two distinct features of closed MCC are its large aspect ratio and its asymmetric circulation pattern (i.e., wide updrafts and narrow downdrafts). Cloud-top radiative cooling may be an important process to generate and maintain closed MCC. The effects of cloud-top cooling on closed MCC are studied in this paper, through linear, weakly nonlinear, and fully nonlinear analyses, using a two-dimensional Boussinesq model with constant-flux upper and lower boundary conditions.

The linear model is unable to represent the effects of cloud-top cooling on the dynamics. Diffusion largely balances out the PE generated by the cloud-top cooling so that there is not enough KE to generate asymmetric circulations such as those observed to be associated with closed MCC. A weakly nonlinear analysis reveals that cloud-top cooling favors the formation of closed MCC. However, the asymmetry of the cells is less than observed due to strong diffusion and weak nonlinearity. Our analysis illustrates, however, that advection near cloud top tends to feed cold air to form narrow downdrafts, suggesting that fully nonlinear processes should be included.

Fully nonlinear numerical simulations show that closed MCC can be driven by cloud-top cooling. Stronger cloud-top cooling results in broader closed MCC. Nonlinear processes associated with the convection, such as mesoscale advection and interactions between convection and the mean state, play essential roles in the formation of closed MCC. Trajectory analyses suggests that concentrated cloud-top cooling, which is able to generate turbulence, and a stable layer near the midlevel, which is able to suppress small-scale convection, are the elements necessary to generate mesoscale circulations.

Based on our numerical results, we have proposed a conceptual model for the formation of closed MCC. Cloud-top cooling, together with a weak stable layer inside a STBL, offer a favorable environment for the formation of closed MCC. Cloud-top cooling generates small-scale turbulence, while the weak stable layer suppresses penetrative small-scale convection. The width of the cells is determined by the distance required to "recharge" the buoyancy of the cooled parcels. Once mesoscale convection has been initiated, it enhances downdrafts by supplying cold air at their tops, helps build up the potential energy that is lost in the sinking motions, and enhances the mesoscale circulations. This conceptual model includes processes that are often observed in the STBL, such as cloud-top cooling, weak surface heating, solar warming, and drizzle, to work together to generate and maintain closed MCC.

That the radiative cooling can drive closed MCC is proved by the weakly nonlinear theoretical analysis, no matter whether it is in a 2D or 3D model. Our further numerical analyses suggest that a 2D energy anticascade does not play an important role in generating the mesoscale circulations in our model. Instead, the mesoscale circulations interact with the mesoscale component of the buoyancy forcing, according to the dynamics and thermodynamics of our model. All of these results suggest that a 2D model is sufficient for our study.

Further evaluation by comparison with observations is necessary. In the real world, the circulation patterns of closed MCC may differ from those simulated here. We expect, however, that the circulations generated by cloud-top cooling are similar to those that we have produced with our model. Our analysis shows that the effects of cloud-top cooling on dynamics cannot be fully represented in the linear and weakly nonlinear regimes.

A quantitative comparison of our numerical results with observations of a STBL is prevented by the simplicity of our model. Moisture, interactive radiation, and realistic upper and lower boundary conditions are all important in a STBL. A further study using a more complex model is an interesting subject for the future.

Acknowledgments. We thank Dr. R. E. Dickinson and the anonymous reviewers for their valuable comments. The satellite image shown in Fig. 1 was provided by Dr. B. A. Wielicki of NASA Langley. Support for this research was provided by NASA's Climate Program under Grant NAG1-1137 and by the Office of Naval Research under Contract N00014-89-J-1364. Qingqiu Shao has also been supported by NSF Grant ATM9113163 and is currently supported by ATM9419715.

APPENDIX

The Filter Used to Select Mesoscale Contributions

The $(2N + 1)$ point running average gives the filter function as (Hamming 1983)

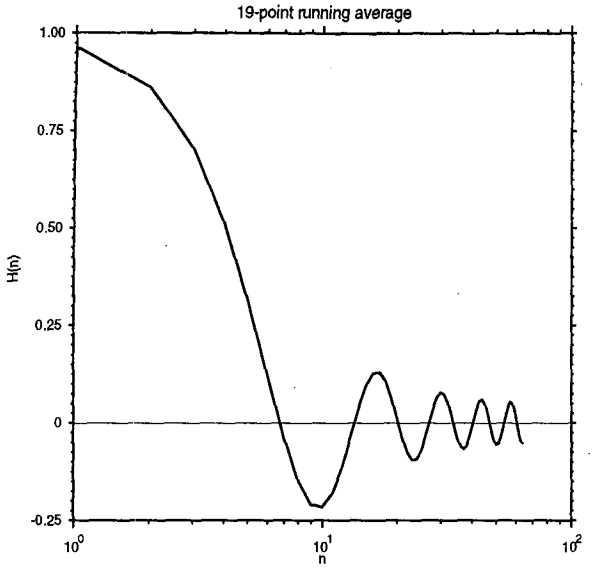

FIG. A1. The profile of the filter used to select the mesoscale contributions.

$$H(n) = \frac{\sin\left[2\pi n\left(N + 1/2\right)/N_0\right]}{(2N + 1)\sin(\pi n/N_0)}, \quad \text{(A1)}$$

where N_0 is the total number of horizontal grid points, n is the wavenumber defined as $n = L/\lambda$, L is the domain size, and λ is the wavelength. For a 19-point running average, $N = 9$. The profile of $H(n)$ is given in Fig. A1. Aliasing error exists with this filter. Waves with wavenumbers larger than six are strongly damped.

REFERENCES

Agee, E. M., 1987: Mesoscale cellular convection over the oceans. *Dyn. Atmos. Oceans*, **10,** 317–341.

——, and F. E. Lomax, 1978: Structure of the mixed layer and inversion layer associated with patterns of mesoscale cellular convection during AMTEX 75. *J. Atmos. Sci.*, **35,** 2281–2301.

——, T. S. Chen, and K. E. Dowell, 1973: A review of mesoscale cellular convection. *Bull. Amer. Meteor. Soc.*, **54,** 1004–1012.

Albrecht, B. A., C. S. Bretherton, D. Johnson, W. H. Schubert, and A. S. Frisch, 1995: The Atlantic Stratocumulus Transition Experiment—ASTEX. *Bull. Amer. Meteor. Soc.*, **76,** 889–904.

Arakawa, A., 1966: Computational design for long-term numerical integration of the equations of fluid motion: Two-dimensional incompressible flow. Part I. *J. Comput. Phys.*, **1,** 119–143.

Austin, P., 1995: A linear stability analysis of stratocumulus convection driven by radiative cooling. *Tellus*, **47A,** 259–274.

Beniston, M., 1985: Organization of convection in a numerical mesoscale model as a function of initial and lower boundary conditions. *Beitr. Phys. Atmos.*, **58,** 31–52.

Brandt, A., 1977: Multi-level adaptive solutions to boundary-value problems. *Math. Comp.*, **31,** 333–390.

Burt, W. V., and E. M. Agee, 1977: Buoy and satellite observations of mesoscale cellular convection during AMTEX 75. *Bound.-Layer Meteor.*, **12,** 3–24.

Chandrasekhar, S., 1961: *Hydrodynamic and Hydromagnetic Stability.* Clarenton Press, 654 pp.

Chapman, C. J., and M. R. E. Proctor, 1980: Nonlinear Rayleigh–Benard convection with poorly conducting boundaries. *J. Fluid Mech.*, **101,** 759–782.

Childress, S., M. Levandowsky, and E. A. Spiegel, 1975: Pattern formation in a suspension of swimming micro-organisms: Equations and stability theory. *J. Fluid Mech.*, **63,** 591–613.

Chlond, A., 1988: Numerical and analytical studies of diabatic heating effect upon flatness of boundary layer rolls. *Beitr. Phys. Atmos.*, **61,** 312–329.

Durran, D. R., 1991: The third-order Adams–Bashforth method: An attractive alternative to leapfrog time differencing. *Mon. Wea. Rev.*, **119,** 702–720.

Fiedler, B. H., 1989: Scale selection in nonlinear thermal convection between poorly conducting boundaries. *Geophys. Astrophys. Fluid Dyn.*, **46,** 191–201.

——, 1990: Transitions to broad cells in a nonlinear thermal convection system. *Geophys. Astrophys. Fluid Dyn.*, **50,** 195–201.

——, 1993: Cell broadening in three-dimensional thermal convection between poorly conducting boundaries. *Beitr. Phys. Atmos.*, **66,** 173–181.

——, and S. Peckman, 1992: Numerical study of convective scale selection in a cloud-topped marine boundary layer. *Tellus*, **44A,** 366–380.

——, and M. Khairoutdinov, 1994: Cell broadening in three-dimensional thermal convection between poorly conducting boundaries. *Beitr. Phys. Atmos.*, **67,** 235–241.

Hamming, R. W., 1983: *Digital Filters.* Prentice-Hall, 257 pp.

Helfand, H. M., and E. Kalnay, 1983: A model to determine open or closed cellular convection. *J. Atmos. Sci.*, **40,** 631–650.

Hubert, L. F., 1966: Mesoscale cellular convection. Meteor. Satellite Lab., NOAA, Rep. 37, ESSA, Washington, DC, 68 pp.

Hurle, D. T. J., E. Jakeman, and E. R. Pike, 1967: On the solution of the Benard problem with boundaries of finite conductivity. *Proc. Roy. Soc. London, Ser. A*, **296,** 469–475.

Kraichnan, R. H., 1967: Inertial ranges in two-dimensional turbulence. *The Physics of Fluids, Suppl. II,* Ameri. Inst. Phys., 233–239.

Krishnamurti, R., 1975: On cellular cloud patterns. Part I: Mathematical model. *J. Atmos. Sci.*, **32,** 1353–1363.

Kropfli, R. A., and B. W. Orr, 1993: Observations of microcells in the marine boundary layer with 8-mm wavelength Doppler radar. Preprints, *26th Int. Conf. on Radar Meteorology,* Norman, OK. Amer. Meteor. Soc., 492–497.

Krueger, A. F., and S. Fritz, 1961: Cellular cloud patterns revealed by TIROS I. *Tellus*, **13,** 1–7.

Lenschow, D. H., and E. M. Agee, 1976: Preliminary results from the Air Mass Transformation Experiment. *Bull. Amer. Meteor. Soc.*, **57,** 1346–1355.

Lilly, D. K., 1968: Models of cloud-topped mixed layers under a strong inversion. *Quart. J. Roy. Meteor. Soc.*, **94,** 292–309.

——, 1969: Numerical simulation of two-dimensional turbulence. *The Physics of Fluids, Suppl. II,* Amer. Inst. Phys., 240–249.

Nicholls, S., and J. Leighton, 1986: An observational study of the structure of stratiform cloud sheets. Part I: Structure. *Quart. J. Roy. Meteor. Soc.*, **112,** 431–460.

Rand, H. A., 1995: Mesoscale dynamics of the marine atmospheric boundary layer. Ph. D. thesis, University of Washington, Seattle, WA, 136 pp.

Randall, D. A., 1980: Conditional instability of the first kind, upside-down. *J. Atmos. Sci.*, **37,** 125–130.

Rothermel, J., and E. M. Agee, 1980: Aircraft investigation of mesoscale cellular convection during AMTEX 75. *J. Atmos. Sci.*, **37,** 1027–1040.

——, and ——, 1986: A numerical study of atmospheric convective scaling. *J. Atmos. Sci.*, **43,** 1185–1197.

Sasaki, Y., 1970: Influences of thermal boundary layer on atmospheric cellular convection. *J. Meteor. Soc. Japan*, **48,** 492–502.

Shao, Q., 1994: The effects of cloud-top processes on convection in the cloud-topped boundary layer. Ph. D. dissertation, Colorado State University, 270 pp.

Sheu, P.- J., E. M. Agee, and J. J. Tribbia, 1980: A numerical study of physical processes affecting convective cellular geometry. *J. Meteor. Soc. Japan,* **58,** 489–499.

Slingo, A., R. Brown, and C. L. Wrench, 1982: A field study of nocturnal stratocumulus: III. High-resolution radiative and microphysical observations. *Quart J. Roy. Meteor. Soc.,* **108,** 145–165.

Sparrow, E. M., R. J. Goldstein, and V. K. Jonsson, 1964: Thermal instability in a horizontal fluid layer: effect of boundary conditions and non-linear temperature profile. *J. Fluid Mech.,* **18,** 513–528.

Sykes, R. I., W. S. Lewellen, and D. S. Henn, 1988: A numerical study of the development of cloud-street spacing. *J. Atmos. Sci.,* **45,** 2556–2569.

Takacs, L. L., 1985: A two-step scheme for the advection equation with minimized dissipation and dispersion errors. *Mon. Wea. Rev.,* **113,** 1050–1065.

van der Borght, R., and E. M. Agee, 1978: Non-linear convection in a moist atmospheric layer heated from below. *J. Meteor. Soc. Japan,* **56,** 284–292.

Zeng, X., and R. A. Pielke, 1993: Error-growth dynamics and predictability of surface thermally induced circulations. *J. Atmos. Sci.,* **50,** 2817–2844.